

University of Illinois at Urbana-Champaign



Air Conditioning and Refrigeration Center A National Science Foundation/University Cooperative Research Center

Experimental and Simulation Analysis of Microchannel Evaporators

S. Song and C. W. Bullard

ACRC CR-47

March 2002

For additional information:

Air Conditioning and Refrigeration Center
University of Illinois
Mechanical & Industrial Engineering Dept.
1206 West Green Street
Urbana, IL 61801

(217) 333-3115

*Prepared for
The Trane Company
and Modine Manufacturing Company*

The Air Conditioning and Refrigeration Center was founded in 1988 with a grant from the estate of Richard W. Kritzer, the founder of Peerless of America Inc. A State of Illinois Technology Challenge Grant helped build the laboratory facilities. The ACRC receives continuing support from the Richard W. Kritzer Endowment and the National Science Foundation. The following organizations have also become sponsors of the Center.

Alcan Aluminum Corporation
Amana Refrigeration, Inc.
Arçelik A. S.
Brazeway, Inc.
Carrier Corporation
Copeland Corporation
Dacor
Daikin Industries, Ltd.
Delphi Harrison Thermal Systems
General Motors Corporation
Hill PHOENIX
Honeywell, Inc.
Hydro Aluminum Adrian, Inc.
Ingersoll-Rand Company
Kelon Electrical Holdings Co., Ltd.
Lennox International, Inc.
LG Electronics, Inc.
Modine Manufacturing Co.
Parker Hannifin Corporation
Peerless of America, Inc.
Samsung Electronics Co., Ltd.
Tecumseh Products Company
The Trane Company
Valeo, Inc.
Visteon Automotive Systems
Wolverine Tube, Inc.
York International, Inc.

For additional information:

*Air Conditioning & Refrigeration Center
Mechanical & Industrial Engineering Dept.
University of Illinois
1206 West Green Street
Urbana, IL 61801*

217 333 3115

Abstract

Microchannel condensers have dominated the automotive a/c market by maximizing performance for a fixed size and weight, but must operate as evaporators if they are to be used in heat pumps. This report presents a microchannel evaporator model, along with experimental validation. The new model structure provides a user-friendly interface and makes it much easier to have good initial guesses. Two different approaches for predicting wetted surface heat and mass transfer are discussed and compared, and the effects of inlet humidity and inclination angle were explored experimentally.

Superheat measurements were used, together with the model to detect significant refrigerant maldistribution that reduced capacity approximately 3%. Frost patterns were used to observe two-phase flow distribution in a microchannel evaporator, and the balance between inertial, gravitational and shear forces was investigated for the vertical headers.

TABLE OF CONTENTS

	Page
Abstract	ii
List of Figures	v
List of Tables	vii
Chapter 1 Evaporator Model Development and Validation	1
1.1 Model structure	1
1.2 Model validation	3
1.2.1 Heat transfer and pressure drop correlations.....	3
1.2.2 Validation results	5
Chapter 2 Model Methods for Wetted Surface Evaporator	7
2.1 Temperature and humidity ratio driving potential.....	7
2.1.1 Fundamental equations	7
2.1.2 Finite element method.....	8
2.1.3 McQuiston’s method.....	8
2.2 Enthalpy driving potential	9
2.2.1 Fundamental equations	9
2.2.2 Analogy between dry and wet heat transfer equations	11
2.2.3 Logarithmic mean enthalpy method.....	12
2.2.4 ϵ -NTU method.....	13
2.2.5 Summary of assumptions for both enthalpy driving potential methods.....	13
2.3 Comparison and discussion	15
2.3.1 Predicted total capacity comparison of different methods.....	15
2.3.2 Discussion of logarithmic mean temperature/humidity difference between air and surface	17
2.3.3 Sensible and latent heat separation for enthalpy potential method	18
Chapter 3 Refrigerant Mass Flow Distribution for MAC2 Indoor Heat Exchanger in Cooling Mode	20
3.1 Introduction	20
3.2 Approach	21
3.3 Experimental design	21
3.3.1 Very large superheated area does not help to determine the distribution	21
3.3.2 Another kind of bad test condition.....	24
3.3.3 Ideal test condition.....	25
3.4 Results and analysis.....	26
3.4.1 Experimental data	26
3.4.2 Model results assuming ideal refrigerant distribution	26
3.4.3 Maldistribution analysis	27
3.5 Conclusion	31
Chapter 4 Analysis of the Inclination Angle Experiment	32
4.1 Introduction.....	32

4.2 Experimental set up	33
4.2.1 Test heat exchanger	33
4.2.2 Test apparatus	33
4.2.3 Test methods.....	34
4.3 Experimental Results	35
4.3.1 Effect of inclination angle on air side heat transfer	35
4.3.2 Effect of inclination angle on air side pressure drop	52
Chapter 5 Frost Deposition and Refrigerant Distribution in Microchannel Heat Exchangers.....	55
5.1 Introduction.....	55
5.2 Experimental facilities.....	56
5.3 Heat exchanger	58
5.4 Heat transfer and refrigerant pressure drop test under dry surface condition	60
5.5 Frosting test	63
5.6 Conclusion	72
References.....	73

List of Figures

	Page
Figure 1.1 Main program structure	1
Figure 1.2 Evaporator model data flow.....	2
Figure 1.3 Comparison of calculated and measured capacities under dry test conditions.....	5
Figure 1.4 Comparison of calculated and measured refrigerant pressure drops under dry test conditions.....	5
Figure 1.5 Comparison of calculated and measured capacities under wet test conditions.....	6
Figure 1.6 Comparison of calculated and measured sensible capacities under wet test conditions.....	6
Figure 2.1 Schematic of finite element method.....	8
Figure 2.2 Enthalpy of saturated air as a function of temperature for standard atmospheric pressure	15
Figure 2.3 b as a function of temperature for standard atmospheric pressure.....	15
Figure 2.4 Capacity comparison using different methods	16
Figure 2.5 Comparison of sensible heat between finite element method (N=20) and logarithmic mean temperature difference between air and surface method.....	17
Figure 2.6 Comparison of latent heat between finite element method and logarithmic mean humidity difference between air and surface method.....	18
Figure 3.1 Arrangement of refrigerant circuits and thermocouples. #1--#4 refer to the four refrigerant circuits.....	20
Figure 3.2 Evaporator configuration	21
Figure 3.3 Refrigerant and air temperature distribution in Test1	23
Figure 3.4 Effect of halving the refrigerant flow rate in Test1	24
Figure 3.5 Refrigerant and air outlet temperature distribution for the bad test condition.....	25
Figure 3.6 Refrigerant and air outlet temperature distribution under ideal test condition.....	26
Figure 3.7 Refrigerant and air outlet temperature distribution assuming ideal distribution	27
Figure 3.8 Refrigerant and air outlet temperature distribution in circuit 1	28
Figure 3.9 Refrigerant and air outlet temperature distribution in circuit 2	28
Figure 3.10 Maldistribution effect on refrigerant exit temperature.....	29
Figure 3.11 Maldistribution effect on capacity.....	30
Figure 3.12 Maldistribution effect on air average outlet temperature	30
Figure 3.13 Maldistribution effect on refrigerant inlet quality	31
Figure 4.1 Schematic diagram of test apparatus.....	34
Figure 4.2 Schematic diagram of heat exchanger installation when the inclination angles were 0°, 14°, 45° and 60°	35
Figure 4.3 Schematic diagram of heat exchanger installation when the inclination angle was 67°	35
Figure 4.4 Chamber capacity versus glycol capacity under dry condition	37
Figure 4.5 Chamber capacity versus air side capacity under dry condition	38
Figure 4.6 Elements along the glycol flow direction.....	41
Figure 4.7 Angle effect on h_a under dry condition using 1-D finite element, LMTD method.....	42
Figure 4.8 Chamber capacity vs. glycol side capacity under wet condition.....	44
Figure 4.9 Chamber capacity vs. air side capacity under wet condition	45

Figure 4.10 Angle effect on air side heat transfer coefficient under wet surface condition using 1-D finite element, NTU method.....	47
Figure 4.11 Element number along the depth of the heat exchanger.....	47
Figure 4.12 Angle effect on air side heat transfer coefficient under wet surface condition using separation of sensible and latent heat method.....	49
Figure 4.13 Calculated vs. measured sensible heat.....	49
Figure 4.14 Calculated vs. measured sensible heat.....	50
Figure 4.15 Water draining effect	51
Figure 4.16 Angle effect on air side pressure drop	52
Figure 4.17 Relationship between the louvers and the airflow direction	53
Figure 4.18 Inlet humidity effect on the air side pressure drop	54
Figure 5.1 Test facilities for R744 prototype residential split system	57
Figure 5.2 Outdoor unit of the prototype R744 heat pump system.....	58
Figure 5.3 Schematic of outdoor heat exchanger.....	59
Figure 5.4 Comparison of calculated air side heat transfer coefficient with Chang & Wang correlation	61
Figure 5.5 Comparison of calculated and measured capacities when the test heat exchanger served as a gas cooler in cooling mode.....	61
Figure 5.6 Energy balance agreement	62
Figure 5.7 Air flow rate and average air pressure drop across the slab A with higher inlet quality (approximately 0.3), keeping blower speed constant.....	64
Figure 5.8 Refrigerant inlet and outlet temperature for slab A with higher inlet quality (approximately 0.3).....	64
Figure 5.9 Sensible capacity for slab A with higher inlet quality (approximately 0.3)	64
Figure 5.10 Frosting of a slab A (right slab) with higher inlet quality at approximately 0.3	68
Figure 5.11 Frosting of a slab A (right slab) with lower inlet quality at approximately 0.1	69
Figure 5.12 Refrigerant inlet and outlet temperature for slab A with lower inlet quality (approximately 0.1).....	70
Figure 5.13 Sensible capacity for slab A with lower inlet quality (approximately 0.1)	70
Figure 5.14 Frosting of a slab B (middle slab)	71

List of Tables

	Page
Table 2.1 Conditions assumed to compare methods for wetted surface	16
Table 3.1 Experimental data with refrigerant exit highly superheated.....	22
Table 3.2 Model result for Test 1	22
Table 3.3 Model result for Test1 after reducing the refrigerant flow rate	23
Table 3.4 Example for one bad test condition	24
Table 3.5 Ideal test condition.....	25
Table 3.6 Experimental data for one refrigerant distribution test.....	26
Table 3.7 Model results assuming ideal distribution condition	27
Table 3.8 Model result of maldistribution for circuit 1 and circuit 2.....	28
Table 4.1 Geometry of the test heat exchanger	33
Table 5.1 Dimensions and characteristics of outdoor heat exchanger.....	60
Table 5.2 Test conditions for outdoor heat exchanger in heating mode.....	60
Table 5.3 Uncertainties of measured and calculated parameters	61
Table 5.4 Test conditions for the slab A and B	62
Table 5.5 Refrigerant pressure drop comparison between slab A and B	63
Table 5.6 Capacity and air side heat transfer coefficient comparison between slab A and B	63

Chapter 1 Evaporator Model Development and Validation

The simultaneous micro-channel evaporator simulation model was initially built by Yin (1999) using Engineering Equation Solver (EES, Klein and Alvarado, 1999). However, the program had two prominent limitations. One is that many initial guesses were required, sometimes for obscure values, which caused great burden on the user. The other is that it lacked a clear model structure. A good heat exchanger model structure is important and necessary due to complex heat exchanger geometries, different refrigerant flow configurations and alternative correlations. Based upon this simultaneous model, the evaporator model with new model structure was developed. The number of initial guess values was reduced substantially, also the model was made clearer and easier to use.

To create a structure for the heat exchanger modeling, the new nomenclature of a 'module' was developed. A module is defined generally as portion, or sub-heat exchanger, part of a larger complex heat exchanger. A heat exchanger can be defined by any number of modules.

Each module is a crossflow heat exchanger that is divided into many small elements. Each element is solved sequentially by a series of heat transfer equations that utilize an ϵ -NTU method. This method reduces, but does not completely eliminate the simultaneous nature of the heat exchanger equations for each element. The remaining implicit, if any, equations are solved with small successive substitution algorithms within each element.

1.1 Model structure

The evaporator simulation model consists of several parts: *Main Program*, *EvapCal Procedure*, *Choose Procedure*, several *Element-solving Procedures*, a *User Library* including all general procedures and functions calculating fin efficiency, heat transfer coefficient, etc.

Main Program is the interface between the user and model. The structure of *Main Program* is shown in Figure 1.1. The inputs for *Main Program* consist of several parts: the geometry inputs; the operating condition inputs; the number of elements and others. After receiving these inputs, the main program calls *GeometryCal Procedure* and *AreaCal Procedure* to calculate the geometry and area parameters, then it calls *EvapCal Procedure* and passes all the necessary information to the latter.

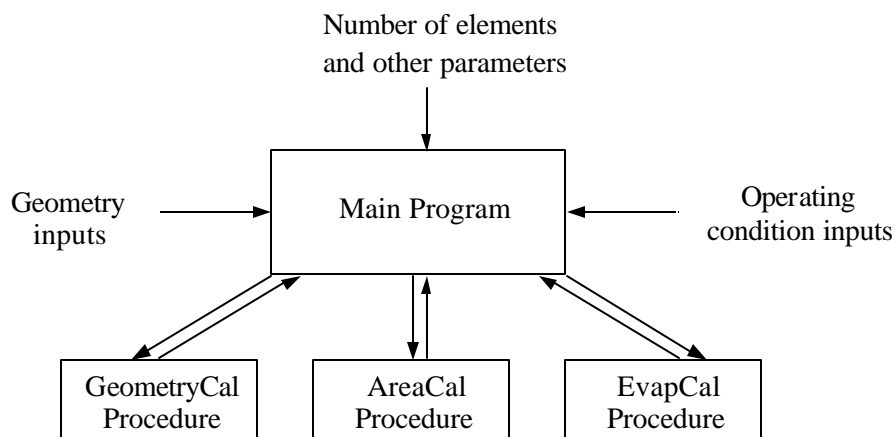


Figure 1.1 Main program structure

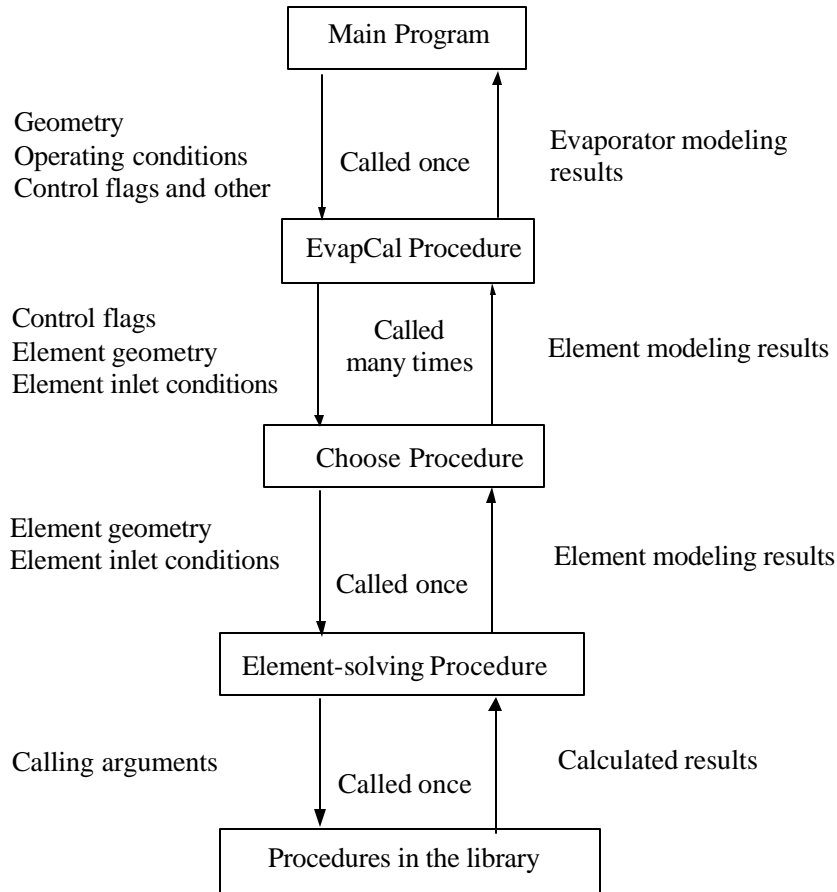


Figure 1.2 Evaporator model data flow

Figure 1.2 shows the data flow for the evaporator model. As shown in Figure 1.2 the program runs in the following way.

User specifies the heat exchanger geometry, operating conditions, control flags and other useful information required by *Main Program* through a parametric table.

Main Program calls *GeometryCal Procedure* and *AreaCal Procedure* to calculate the geometry and area parameters, then it calls *EvapCal Procedure* and passes all the necessary information to the latter.

The heat exchanger circuiting is set in *EvapCal Procedure*. *EvapCal Procedure* calls *Choose Procedure* repeatedly depending on the amount of the elements when it marches through the heat exchanger. The geometry information and inlet conditions of each element, and forward-control-flag (defined below) are passed to *Choose Procedure*.

The inlet condition of each element is checked by *Choose Procedure* to determine if this element is in two-phase zone or superheat zone. Then *Choose Procedure* does some calculation to find out if the surface is totally dry, totally wet or partially dry partially wet. Then it chooses and calls the appropriate *Element-solving Procedure*.

Once called by *Choose Procedure*, an *Element-solving Procedure* gets the element geometry parameters and inlet conditions from *Choose Procedure* and calculates the heat transfer and refrigerant pressure drop etc. for the element.

During this process, *Element-solving Procedure* calls general procedures and functions in the *User Library* when needed.

After each element is simulated, the results are returned from *Element-solving Procedure* to *EvapCal Procedure* through *Choose Procedure* and stored in an array in *EvapCal Procedure*.

After completing the calculation for all the elements, the final results are summarized in *EvapCal Procedure*, such as the predicted total heat transfer rate, refrigerant exit quality etc. Then they are transferred to *Main Program*.

Some parameters are defined as input and others output in the procedures, and they are fixed while executing the program. However, from the user's perspective there are several groups containing certain kinds of parameters, and the parameters in the same group are interchangeable. That is, given some of the parameters, no matter they are defined as input or output in the procedure, the procedure can calculate the corresponding interchangeable parameters due to the capability of EES solving equations simultaneously.

There is one control flag set in the *Main Program*, forward-control flag. It is part of the input arguments of the *EvapCal Procedure*. The model always marches downwind and the forward-control flag specifies the marching direction: upstream marching or downstream marching.

1.2 Model validation

The validation of the new evaporator model was conducted using experimental data from the second generation of a CO₂ mobile air conditioning system with a micro-channel evaporator. The details about the test facility refer to Giannavola and Hrnjak (2001). The details of the heat exchanger description refer to Chapter 3.

1.2.1 Heat transfer and pressure drop correlations

The air side heat transfer correlation selected for the model was proposed by Chang and Wang (1997). It was selected because it covered the widest array of geometries and is one of the most recently published louvered fin air side heat transfer coefficient correlations.

The Chang and Wang correlation was defined in terms of the dimensionless heat transfer coefficient, the Colburn j-factor:

$$j = \text{Re}_{Lp}^{-0.49} \left(\frac{q}{90} \right)^{0.27} \left(\frac{Fp}{Lp} \right)^{-0.14} \left(\frac{Fl}{Lp} \right)^{-0.29} \left(\frac{Td}{Lp} \right)^{-0.23} \left(\frac{Ll}{Lp} \right)^{0.68} \left(\frac{Tp}{Lp} \right)^{-0.28} \left(\frac{df}{Lp} \right)^{-0.05} \quad (1.1)$$

The above correlation can be used in the Reynolds number range from 100 to 3000 based on the louver pitch. The Reynolds number of our experimental data lay between 125 and 540.

Hwang's correlation (1997) was selected for the refrigerant side heat transfer calculation in the model since it was developed based on CO₂ evaporation tests:

$$h_r = h_{nb} + h_{cv} \quad (1.2)$$

$$h_{nb} = 0.0012S \left(\frac{k_l^{0.79} c P_l^{0.5} r_l^{0.49}}{s^{0.6} m_l^{0.29} r_{lv}^{0.24} r_v^{0.24}} \right) [T_w - T_{sat}(P_l)]^{0.4} [P_{sat}(T_w) - P_l]^{0.75}$$

$$S = \frac{1 - \exp(-F h_l X_o / k_l)}{F h_l X_o / k_l} \quad (1.3)$$

$$X_o = 0.05 \left(\frac{s}{g(r_l - r_v)} \right)^{0.5}$$

$$h_{cv} = h_l F Pr_l^{0.6} \quad (1.4)$$

$$F = 1.0 \quad \text{for } X_{tt} \geq 10$$

$$F = 2.0(0.2113 + 1/X_{tt}) \quad \text{for } X_{tt} < 10 \quad (1.5)$$

$$X_{tt} = \left(\frac{1-x}{x} \right)^{0.875} \left(\frac{r_v}{r_l} \right)^{0.5} \left(\frac{m_l}{m_v} \right)^{0.125} \quad (1.6)$$

Refrigerant two-phase pressure drop can be expressed as sum of pressure drops due to friction and momentum change:

$$\Delta P_{tp} = \Delta P_f + \Delta P_m \quad (1.7)$$

Pressure drop due to friction is

$$\Delta P_f = \Delta P_{lo} \left[\frac{1}{\Delta x} \int f_{lo}^2 dx \right]$$

$$\Delta P_{lo} = \frac{2 f_{lo} G^2 L}{r_l d} \quad (1.8)$$

Where f_{lo} is the liquid Fanning friction coefficient.

Two-phase multiplier, Φ_o is expressed as (Souza and Pimenta, 1995):

$$f_{lo}^2 = 1 + (\Gamma^2 - 1) x^{1.75} \left(1 + 0.9524 \Gamma X_{tt}^{0.4126} \right) \quad (1.9)$$

$$\Gamma = (r_l / r_v)^{0.5} (m_v / m_l)^{0.125} \quad (1.10)$$

Pressure drop due to momentum change can be defined as:

$$\Delta P_m = G^2 \left[\left\{ \frac{x_e^2}{r_v a_e} + \frac{(1-x_e)^2}{r_l (1-a_e)} \right\} - \left\{ \frac{x_i^2}{r_v a_i} + \frac{(1-x_i)^2}{r_l (1-a_i)} \right\} \right] \quad (1.11)$$

Where α is void fraction (Zivi, 1964):

$$a = \frac{1}{1 + \left(\frac{1-x}{x} \right) \left(\frac{r_v}{r_l} \right)^{0.67}} \quad (1.12)$$

1.2.2 Validation results

1.2.2.1 Dry surface

A series of tests were run under dry test conditions for indoor heat exchanger in cooling mode. The range of air face velocity is from 1.7 m/s to 7.0 m/s.

Energy balance was measured by three independent methods (chamber, refrigerant and air side). The chamber capacity measurement is always has smaller uncertainty than the other two capacity measurements. So chamber capacity is used to compare with the model results. Figure 1.3 to 1.4 compare the model predictions with the measured data. As shown in Figure 1.3, the model predicts the capacity within $\pm 3\%$. Figure 1.4 shows that the model systematically underpredicted the refrigerant pressure drop. For a similar heat exchanger subjected to extensive nitrogen flow testing, Yin *et al* (2000) found the average port diameter to be 94% of nominal and that 39% of ports were blocked. These estimates were confirmed by dismantling the heat exchanger, measuring port diameters and counting the number of ports blocked by brazing flux. Therefore blocked ports might explain the disparity between the model prediction and pressure drop data.

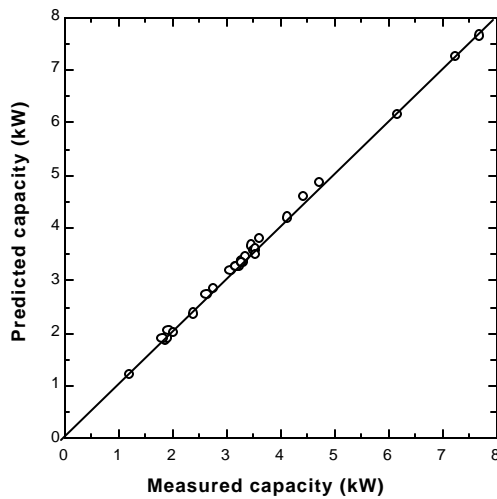


Figure 1.3 Comparison of calculated and measured capacities under dry test conditions

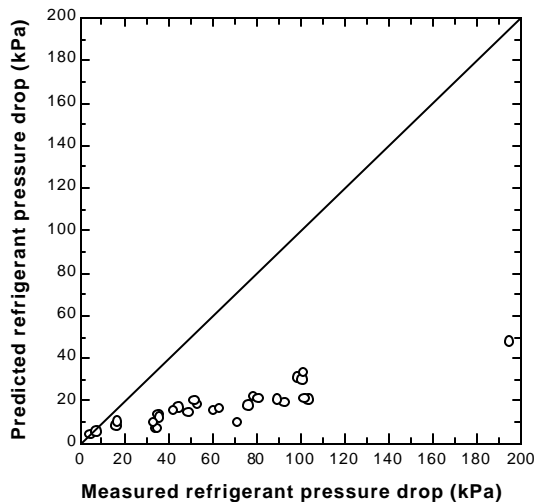


Figure 1.4 Comparison of calculated and measured refrigerant pressure drops under dry test conditions

1.2.2.2 Wet surface

The model method for wet surface is discussed in detail in Chapter 2. Figure 1.5 to 1.6 compare the model predictions with the measured data. As Figure 1.5 and 1.6 illustrate, the simulation model predictions of total capacity and sensible capacity are all scattered about the zero error line in a fairly narrow range.

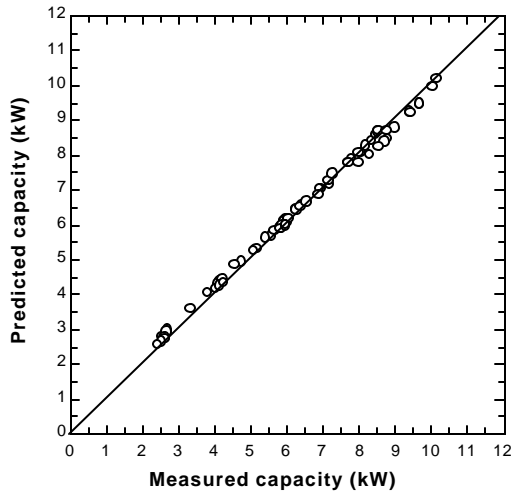


Figure 1.5 Comparison of calculated and measured capacities under wet test conditions

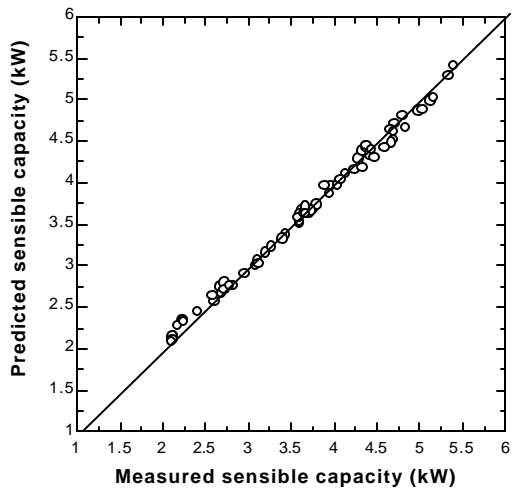


Figure 1.6 Comparison of calculated and measured sensible capacities under wet test conditions

1.2.2.3 Validation summary

The agreement between the model predictions and the experimental data confirm the validity of the new model structure. This evaporator model will be embedded in the simulation system in the future work.

Chapter 2 Model Methods for Wetted Surface Evaporator

In this chapter, two different approaches for predicting wetted surface heat and mass transfer are discussed. The first approach uses temperature and humidity ratio driving potentials for heat and mass transfer, and determines surface temperature directly. The second approach makes use of a moist air enthalpy-based driving potential.

2.1 Temperature and humidity ratio driving potential

2.1.1 Fundamental equations

The rate of sensible heat transfer from the water surface to the air q_s can be calculated by the one-dimensional convection equation

$$dq_s = h_c dA_a (t_a - t_p) \quad (2.1)$$

Where q_s = rate of sensible heat transfer, W

h_c = convection coefficient, W/m²·K

t_p = wetted surface temperature, °C

t_a = air temperature, °C

The transfer of heat due to the evaporation

$$dq_l = h_D dA_a (w_a - w_p) h_{fg} \quad (2.2)$$

Where q_l = rate of latent heat transfer, W

h_D = mass transfer proportionality constant, kg/m²·s

w_p = humidity ratio of saturated air at wetted-surface temperature

h_{fg} = latent heat of water at wetted-surface temperature, J/kg

There exists a proportional relation between h_D and h_c

$$h_D = \frac{h_c}{C_{p,m} Le^{2/3}} \quad (2.3)$$

Where $C_{p,m}$ is the specific heat of moist air, J/kg·K

The use of the heat and mass transfer analogy results in the following relation for the heat transfer rate to the surface:

$$dq_t = dq_s + dq_l = h_c dA_a (t_a - t_p) + \frac{h_c}{C_{p,m} Le^{2/3}} dA_a (w_a - w_p) h_{fg} \quad (2.4)$$

The rate of heat transfer from the refrigerant to the water surface q_t can be calculated as follows

$$dq_t = h_r dA_r (t_p - t_r) \quad (2.5)$$

Where h_r = refrigerant heat transfer coefficient, W/m²·K

t_r = refrigerant temperature, °C

2.1.2 Finite element method

Using finite element method as shown in Figure 2.1, these one-dimensional prediction results should yield an exact solution for the two-dimensional case if the elements are small enough. The tube surface temperature is assumed isothermal for each element.

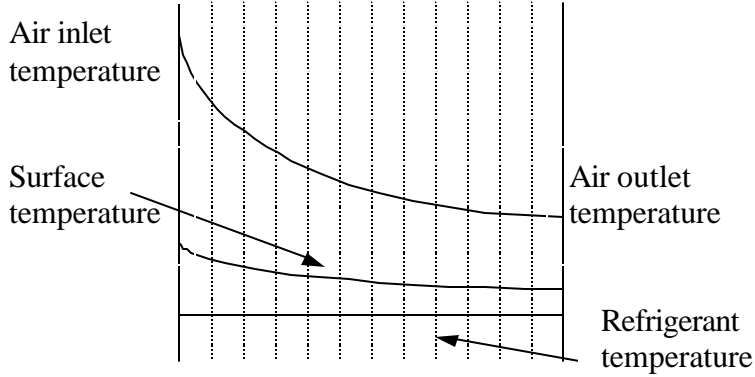


Figure 2.1 Schematic of finite element method

Using Euler's method, the governing equations for each element are the simplest as follows.

Heat transfer between refrigerant and surface

$$Q_t = h_r A_r (t_p - t_r) \quad (2.6)$$

Sensible heat transfer between surface and air

$$Q_s = h_c h_o A_a \left(\frac{t_{a,i} + t_{a,o}}{2} - t_p \right) \quad (2.7)$$

Latent heat transfer between surface and air

$$Q_l = h_D A_a h_o \left(\frac{w_{a,i} + w_{a,o}}{2} - w_p \right) h_{fg} \quad (2.8)$$

2.1.3 McQuiston's method

This method is based upon a suggestion by McQuiston (1975) for calculating the sensible and latent heat transfer rates separately. He suggests that the sensible heat transfer rate is computed in the usual way (the same as for dry surface):

$$Q_s = UA_a h_o \Delta T_{lm} \quad (2.9)$$

$$\Delta T_{lm} = \frac{(t_{a,i} - t_{r,i}) - (t_{a,o} - t_{r,o})}{\ln\left(\frac{t_{a,i} - t_{r,i}}{t_{a,o} - t_{r,o}}\right)}$$

Where

(2.10)

$$\frac{1}{U} = \frac{1}{h_o h_c} + \frac{A_a}{h_r A_r}$$
(2.11)

The latent heat transfer may be computed as follows

$$Q_l = h_D A_a h_o \Delta w_{lm} h_{fg}$$
(2.12)

Assume Δw_{lm} has the same form as ΔT_{lm} :

$$\Delta w_{lm} = \frac{(w_{a,i} - w_{p,i}) - (w_{a,o} - w_{p,o})}{\ln\left(\frac{w_{a,i} - w_{p,i}}{w_{a,o} - w_{p,o}}\right)}$$
(2.13)

It should be noted that Equation 2.9 is strictly valid only for dry surfaces. This restriction is a result of the fact that it is otherwise not possible to relate the sensible heat transfer rate to the air and refrigerant temperatures using a heat transfer resistance network.

Although this model method is simple and straightforward, sometimes it may cause large errors. So this method will not be used to predict the heat exchanger performance in the following discussion.

2.2 Enthalpy driving potential

There are two methods using the enthalpy difference between the moist air and the condensing surface as the driving force. One is logarithmic mean enthalpy method; the other is NTU method. The NTU method is just an alternative computational approach. The underlying physical assumptions and therefore the results of the two methods are the same. Concerning computation, the NTU method converges more easily.

2.2.1 Fundamental equations

The enthalpy potential method can be derived from Equation 2.4:

$$dq_t = dq_s + dq_l = h_c dA_a (t_a - t_p) + \frac{h_c}{C_{p,m} Le^{2/3}} dA_a (w_a - w_p) h_{fg}$$

Rearrangement of this one-dimensional equation yields

$$dq_t = \frac{h_c}{C_{p,m}} \left(\left(C_{p,m} t_a + \frac{h_{fg} w_a}{Le^{2/3}} \right) - \left(C_{p,m} t_p - \frac{h_{fg} w_p}{Le^{2/3}} \right) \right) dA_a$$
(2.14)

Over a small temperature range, the enthalpy of air can be approximated as

$$h_a = C_{p,m} T_a + w_a h_{fg}$$
(2.15)

After some algebraic manipulations, Equation 2.14 and 2.15 lead to the relationship

$$dq_t = \frac{h_c}{C_{p,m}} \left((h_a - h_{s,p}) + (\mathbf{w}_p - \mathbf{w}_a) h_{fg} \left(1 - Le^{2/3} \right) \right) dA_a \quad (2.16)$$

The second term inside the brackets in Equation 2.16 is 3-4% of the total bracketed term. Dropping this term yields the enthalpy potential method of calculating heat transfer to a condensing surface

$$dq_t = \frac{h_c}{C_{p,m}} (h_a - h_{s,p}) dA_a \quad (2.17)$$

Where $h_{s,p}$ = enthalpy of saturated air at the wetted-surface temperature, kJ/kg

Kuehn et al. (1995) used Equation 2.17 as the starting point in deriving the logarithmic mean enthalpy method, which is commonly used to calculate cooling coil performance (ARI 1987, Threlkeld 1970, Stoecker and Jones 1982). Kuehn *et al.* assumes that a moving film of water is formed on the surface by condensation of moisture from the air stream. Equation 2.17 becomes

$$dq_t = \frac{h_c}{C_{p,m}} (h_a - h_{s,w}) dA_a \quad (2.18)$$

Where $h_{s,w}$ = enthalpy of saturated air at the water-air surface temperature t_w , kJ/kg. However the resistance of the water film is often neglected, reverting to Equation 2.17.

Besides Equation 2.18, another relation will be used repeatedly in subsequent sections of this chapter. We will assume that over a small range of temperature, the enthalpy of saturated air h_s may be represented as

$$h_s = a + bt_s \quad (2.19)$$

Assume that heat conduction through the water film occurs in only one direction. We have

$$dq_t = \frac{k_w}{y_w} (t_w - t_p) dA_a \quad (2.20)$$

Where k_w and y_w are, respectively, the thermal conductivity and thickness of the water film. By Equation 2.19

$$dq_t = \frac{k_w}{b_w y_w} (h_{s,w} - h_{s,p}) dA_a \quad (2.21)$$

$$\text{Where } b_w = \frac{h_{s,w} - h_{s,p}}{t_w - t_p} \quad (2.22)$$

By Equation 2.18 and 2.21, we obtain

$$dq_t = \frac{h_{o,w}}{b_w} (h_a - h_{s,p}) dA_a \quad (2.23)$$

$$\text{Where } h_{o,w} = \frac{1}{C_{p,m} / (b_w h_c) + y_w / k_w} \quad (2.24)$$

The local rate of heat transfer inside the tube:

$$dq_t = h_r dA_r (t_p - t_r) \quad (2.25)$$

By definition, let

$$b_R = \frac{h_{s,p} - h_{s,r}}{t_p - t_r} \quad (2.26)$$

Where $h_{s,p}$ and $h_{s,r}$ are fictitious enthalpies of saturated moist air evaluated at the respective temperatures t_p and t_r . By Equation 2.25 and 2.26, we obtain

$$dq_t = \frac{h_r dA_r}{b_R} (h_{s,p} - h_{s,r}) \quad (2.27)$$

The enthalpy change of refrigerant is calculated as follows

$$dq_t = dm_r C_{p,r} (t_{r,o} - t_{r,i}) \quad (2.28)$$

If the refrigerant temperature change is small, we can assume the quantities a_r and b_r as constants in the relation $h_{s,r} = a_r + b_r t_r$. We have

$$dq_t = \frac{dm_r C_{p,r}}{b_r} (h_{s,r,o} - h_{s,r,i}) \quad (2.29)$$

$h_{s,r,i}$ and $h_{s,r,o}$ are, respectively, fictitious enthalpies of saturated air calculated at the entering and leaving refrigerant temperatures.

The enthalpy change of air is calculated as follows

$$dq_t = dm_a (h_{a,i} - h_{a,o}) \quad (2.30)$$

Where $h_{a,i}$ and $h_{a,o}$ are, respectively, the true enthalpies of the entering and leaving air stream.

2.2.2 Analogy between dry and wet heat transfer equations

For dry surface conditions the heat transfer equations are

$$dq_t = h_c (t_a - t_p) dA_a \quad (2.31)$$

$$dq_t = h_r (t_p - t_r) dA_r \quad (2.32)$$

$$dq_t = dm_r C_{p,r} (t_{r,o} - t_{r,i}) \quad (2.33)$$

$$dq_t = dm_a C_{p,a} (t_{a,i} - t_{a,o}) \quad (2.34)$$

For wet surface conditions the heat and mass transfer equations are

$$dq_t = \frac{h_{o,w}}{b_w} (h_a - h_{s,p}) dA_a \quad (2.35)$$

$$dq_t = \frac{h_r dA_r}{b_R} (h_{s,p} - h_{s,r}) \quad (2.36)$$

$$dq_t = \frac{dm_r C_{p,r}}{b_r} (h_{s,r,o} - h_{s,r,i}) \quad (2.37)$$

$$dq_t = dm_a (h_{a,i} - h_{a,o}) \quad (2.38)$$

Comparing the heat transfer equations for dry and wet surface conditions, we find that there is an analogy between the two sets of equations. The difference is that the driving potential is enthalpy difference for wet surface instead of temperature difference for dry surface. We may recall that for dry surface where only sensible heat transfer occurs, temperature difference between the two fluids is given by the logarithmic mean temperature difference, and NTU method is an alternative method. We can also show that by analogy logarithmic mean enthalpy method and NTU method for wet surface can be derived.

2.2.3 Logarithmic mean enthalpy method

We can show that, with certain approximations, for pure counterflow the mean air enthalpy difference is given by

$$Q_t = U_{o,w} A_a LMhD \quad (2.39)$$

$$\text{Where } LMhD = \frac{(h_{a,i} - h_{s,r,i}) - (h_{a,o} - h_{s,r,o})}{\ln \left(\frac{h_{a,i} - h_{s,r,i}}{h_{a,o} - h_{s,r,o}} \right)} \quad (2.40)$$

We may show that

$$U_{o,w} = \frac{1}{\frac{b_R A_a}{A_r h_r} + \frac{b_{w,m} (1 - \mathbf{h}_{F,w})}{h_{o,w} (A_r / A_F + \mathbf{h}_{F,w})} + \frac{b_{w,m}}{h_{o,w}}} \quad (2.41)$$

Where $b_{w,m}$ is evaluated at the mean surface temperature of the water film on the fin. $\mathbf{h}_{F,w}$ is the fin efficiency for wet surface and A_F is the fin area.

2.2.4 ϵ -NTU method

Recall the derivation of ϵ -NTU method for dry surface condition, the ϵ -NTU method for wetted surface condition can also be derived using some analogy.

$$C_r = \frac{C_{\min}}{C_{\max}} = \frac{\min [m_a, (m_r C_{p,r} / b_r)]}{\max [m_a, (m_r C_{p,r} / b_r)]} \quad (2.42)$$

$$\mathbf{e} = 1 - \exp \left\{ \frac{NTU^{0.22}}{C_r} [\exp(-C_r NTU^{0.78}) - 1] \right\} \quad (2.43)$$

If the refrigerant temperature is assumed constant, we have

$$\mathbf{e} = 1 - \exp(-NTU) \quad (2.44)$$

$$NTU = \frac{U_{o,w} A_a}{C_{\min}} \quad (2.45)$$

$$Q_{\max} = m_a (h_{a,i} - h_{s,r}) \quad (2.46)$$

$$Q_t = \mathbf{e} Q_{\max} \quad (2.47)$$

Where $U_{o,w}$ is calculated using Equation 2.41.

2.2.5 Summary of assumptions for both enthalpy driving potential methods

A relatively small term is neglected to obtain that the driving force is the moist air enthalpy difference.

Assume that over a small range of temperature, the enthalpy of saturated air h_s may be represented

$$\text{as } h_s = a + bt_s$$

The two methods are restricted to cases where the refrigerant temperature change is small, since in the derivation it

is necessary to assume the quantities a_r and b_r as constants in the relation $h_{s,r} = a_r + b_r t_r$.

Some error may arise when determining b_R' and $b_{w,m}$ as described below.

The tube surface temperature and mean surface temperature of the water film on the fin usually is not uniform. Some error may arise when determining b_R' and $b_{w,m}$. Fortunately, the evaluation of b_R' and $b_{w,m}$ will not cause big error if these temperatures do not change too much. One way to determine b_R' is to calculate the average tube surface temperature as follows

$$Q_t = h_r A_r (t_{p,avg} - t_{r,avg}) \quad (2.48)$$

b_R' can be calculated using the average surface temperature:

$$b_R' = \frac{h_{s,p,avg} - h_{s,r}}{t_{p,avg} - t_r} \quad (2.49)$$

To establish a procedure to determine $b_{w,m}$, we begin by definition of fin efficiency for wetted surface

$$\mathbf{h}_{F,w} = \frac{h_a - h_{s,p}}{h_a - h_{F,m}} \quad (2.50)$$

Where $h_{F,m}$ is the fictitious saturated enthalpy of moist air evaluated at mean fin temperature $t_{F,m}$.

Make the approximation $h_{F,m} = h_{s,w,m}$ (Resistance of water film is negligible), we have

$$\mathbf{h}_{F,w} = \frac{h_a - h_{s,p}}{h_a - h_{s,w,m}} \quad (2.51)$$

One way to calculate $h_{s,w,m}$ is to use average air enthalpy

$$\mathbf{h}_{F,w} = \frac{h_{a,avg} - h_{s,p}}{h_{a,avg} - h_{s,w,m}} \quad (2.52)$$

$$\text{Where } h_{a,avg} = (h_{a,i} + h_{a,o})/2 \quad (2.53)$$

The derivation of wet fin efficiency is completely analogous to dry fin efficiency. We find that solutions for efficiency of dry fins also apply for efficiency of wet fins if we substitute $h_{o,w}$ for the wet fin in place of h_c for the dry fin.

$$\mathbf{h}_{F,w} = \frac{\tanh mL}{mL} \quad (2.54)$$

$$\text{Where } m = \sqrt{h_{o,w}/(k_F y)} \quad (2.55)$$

Equation 2.52 allows determination of $t_{w,m}$ and therefore $b_{w,m}$ through calculation of the enthalpy of saturated air, $h_{s,w,m}$.

Figure 2.2 shows how nearly the saturated air enthalpy approximates a linear function. And Figure 2.3 shows how b varies with temperature using numerical derivatives.

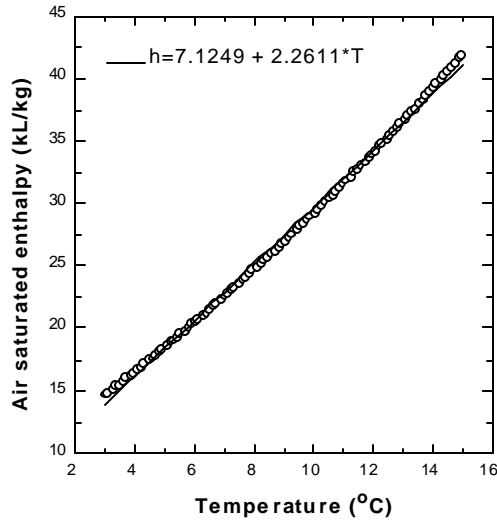


Figure 2.2 Enthalpy of saturated air as a function of temperature for standard atmospheric pressure

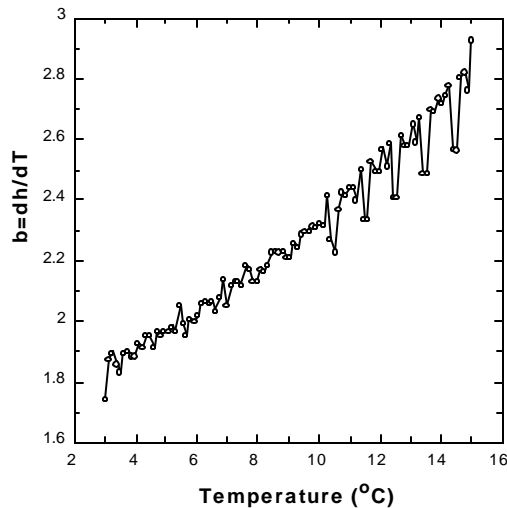


Figure 2.3 b as a function of temperature for standard atmospheric pressure

2.3 Comparison and discussion

2.3.1 Predicted total capacity comparison of different methods

One microchannel crossflow evaporator and one operating condition are chosen to compare the model results using different methods. The airside heat transfer coefficient varies from 50 to 300 W/m²-K to simulate different operating conditions. To facilitate comparison, several assumptions are made as follows: 1) Assume that the refrigerant temperature is constant; 2) The surface efficiency is assumed 1 for all the methods; 3) The fouling factor and wall resistance are negligible; 4) $b_{w,m}$ is evaluated at the average tube surface temperature because the average fin surface temperature is the same as the average tube surface temperature when the surface efficiency is assumed 1. And b_R is calculated using the average tube surface temperature and refrigerant temperature.

The evaporator heat transfer area, airside and refrigerant side heat transfer coefficient and operating condition are shown in Table 2.1.

Figure 2.4 shows that the moist air enthalpy method (including logarithmic mean enthalpy method and NTU method) underestimates total (sensible plus latent) heat transfer by 0.2% to 2% compared with finite element method. The difference is partially due to the assumptions required to derive the logarithmic mean enthalpy relationship (linear relationship between the saturated temperature and enthalpy, ignored small term, evaluation of b). The disparity between the NTU method and LMhD method is very small; the maximum error is 0.03% due to roundoff error. NTU method and LMhD method have the advantage of greater computational efficiency, since the heat exchanger's performance is determined by equations, which require only the inlet and outlet conditions of the two fluid streams, and there is no need to calculate surface temperature explicitly. NTU method has an additional advantage over the LMhD method because the program converges more easily due to the sequential nature of the equations.

Table 2.1 Conditions assumed to compare methods for wetted surface

Heat transfer area	Airside heat transfer area, A_a	4.079m ²
	Refrigerant side heat transfer area, A_r	0.7487m ²
Operating condition	Air inlet temperature, $t_{a,i}$	12.53°C
	Air flow rate, m_a	0.530kg/s
	Air inlet humidity, $W_{a,i}$	0.00743
	Refrigerant temperature, t_r	2.435°C
	Refrigerant flow rate, m_r	0.4793kg/s
Heat transfer coefficient	Refrigerant heat transfer coefficient, h_r	1411W/m ² -K
	Air heat transfer coefficient, h_c	50~300 W/m ² -K

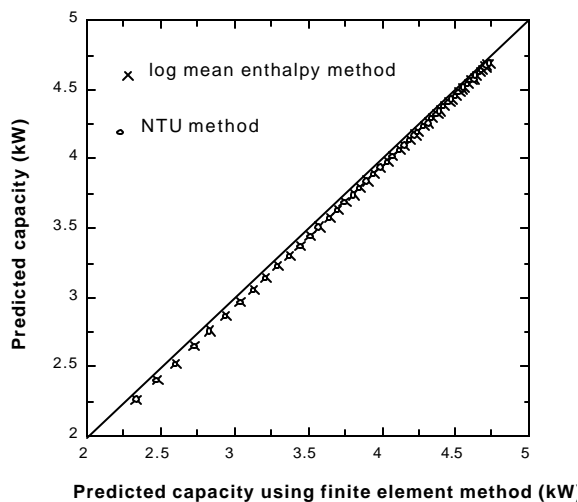


Figure 2.4 Capacity comparison using different methods

2.3.2 Discussion of logarithmic mean temperature/humidity difference between air and surface

Some models and papers did not use the three methods mentioned above, instead, they used logarithmic mean temperature/humidity difference between air and surface as McQuiston did. However, no one has ever quantified the error it introduced. In this part we try to quantify the error under different conditions and to see whether the logarithmic mean temperature/humidity difference is a good approximation or not.

Recall that finite element method can give us the correct prediction results and the temperature/humidity distribution. So

1. The finite element method is used to obtain the “correct” results.
2. The average surface temperature is determined by the heat transfer between refrigerant and tube surface using a one-dimensional approximation.

$$t_{p,avg} = \frac{Q_t}{h_r A_r} + t_r \quad (2.56)$$

Where Q_t is the total heat transfer predicted in #1.

3. The logarithmic mean temperature/humidity difference between air and surface are calculated using the calculated air outlet temperature and humidity in #1 and the average tube surface temperature in # 2.
4. The sensible and latent heat are calculated using the logarithmic mean temperature/humidity difference and compared with the “correct” results. Thus, we can check whether the logarithmic mean temperature/humidity difference calculation between air and surface is a good approximation or not.

Using the same microchannel crossflow heat exchanger and operating conditions in Table 2.1, airside heat transfer coefficient was varied to obtain a wide range of air and refrigerant thermal resistance ratio.

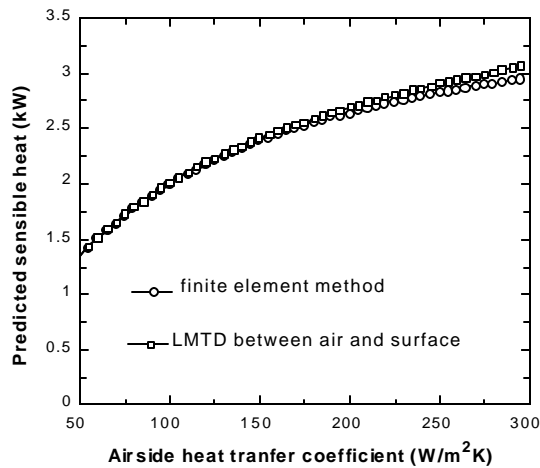


Figure 2.5 Comparison of sensible heat between finite element method (N=20) and logarithmic mean temperature difference between air and surface method

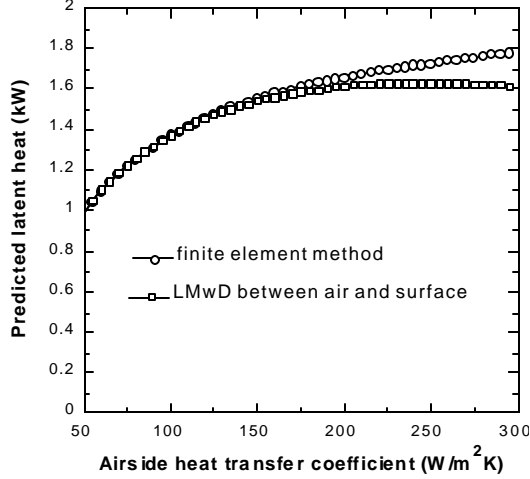


Figure 2.6 Comparison of latent heat between finite element method and logarithmic mean humidity difference between air and surface method

Figure 2.5 and Figure 2.6 show that the logarithmic mean temperature/humidity difference between air and surface is a good approximation when the ratio of air resistance and refrigerant resistance is large. However, the error increases with the decrease of the ratio. To understand this, we begin by writing the relation for the differential area

$$m_a d\mathbf{w}_a = h_D dA_a (\mathbf{w}_a - \mathbf{w}_p) h_{fg} \quad (2.57)$$

$$m_a C_{p,a} dt_a = h_c dA_a (t_a - t_p) \quad (2.58)$$

If the tube surface temperature t_p , thus saturated humidity at the surface, \mathbf{w}_p , is assumed constant, we can find that logarithmic mean temperature/humidity difference between air and surface is valid after integration. If the ratio of air resistance and refrigerant resistance is large, the tube surface temperature is close to refrigerant temperature and almost constant along the evaporator depth. The changes of the tube surface temperature and the saturated humidity at the surface temperature are very small from the leading edge to the trailing edge. The logarithmic mean temperature/humidity difference between air and surface is a good approximation in this case.

2.3.3 Sensible and latent heat separation for enthalpy potential method

We have to separate the sensible and latent capacity for enthalpy potential method after the total capacity is obtained. The simplest way to implement it is to assume that the tube surface temperature is uniform and the average tube surface temperature $t_{p,avg}$ can be determined by Equation 2.56. The arithmetic mean temperature difference between air and surface is used to calculate the sensible capacity.

$$Q_s = h_c A_a h_o \left(\frac{t_{ai} + t_{ao}}{2} - t_{p,avg} \right) \quad (2.59)$$

The latent capacity is backed out

$$Q_l = Q_t - Q_s \quad (2.60)$$

Another way to implement it is to assume that the tube surface temperature is uniform and the average tube surface temperature $t_{p,avg}$ can be determined by Equation 2.56. The arithmetic humidity difference between air humidity and saturated humidity at $t_{p,avg}$ is used to calculate the latent capacity.

$$Q_l = h_D A_a h_o \left(\frac{w_{ai} + w_{ao}}{2} - w_p \right) h_{fg} \quad (2.61)$$

The sensible capacity is backed out

$$Q_s = Q_t - Q_l \quad (2.62)$$

Because latent capacity is almost always smaller than sensible capacity, the second method will introduce smaller relative error by calculating latent capacity first.

Chapter 3 Refrigerant Mass Flow Distribution for MAC2 Indoor Heat Exchanger in Cooling Mode

3.1 Introduction

MAC2 indoor heat exchanger servers as an evaporator in cooling mode with four refrigerant inlets. A conventional conical distributor with four outlets, supplied by Sporlan Valve Company, is used in the MAC2 mobile air-conditioning test facility in order to get uniform refrigerant distribution among the four circuits.

The refrigerant mass flow distribution among the four circuits can be observed by measuring the superheated temperatures of the refrigerant at the four outlets. Identical temperatures may imply a uniform distribution, while different temperatures may indicate a maldistribution. In the latter case, a higher superheated temperature indicates a lower mass flow rate of refrigerant while a lower superheated temperature indicates a higher mass flow rate in the respective circuit.

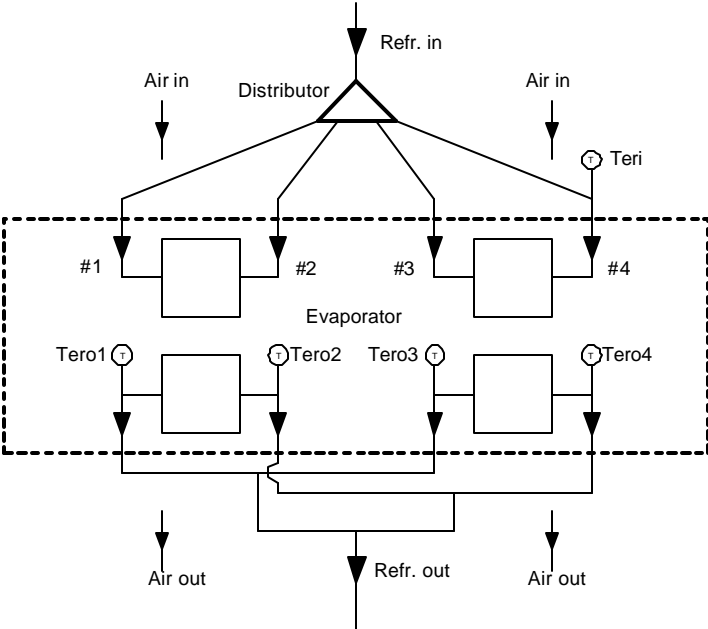


Figure 3.1 Arrangement of refrigerant circuits and thermocouples.
#1--#4 refer to the four refrigerant circuits.

Figure 3.1 shows the arrangement of the distributor and thermocouples. The distributor is connected to the evaporator inlets using four identical copper tubes. Four thermocouples are immersed into the four outlet tubes of the circuits, respectively, measuring the outlet temperatures Tero1, Tero2, Tero3 and Tero4. One thermocouple is placed into one inlet (#4) tube to measure the inlet temperature Teri. The other three inlet temperatures are equal to the measured one because the inlet state of refrigerant is in two-phase and we assume that the pressures at the four inlets are identical.

Figure 3.2 shows the evaporator configuration.

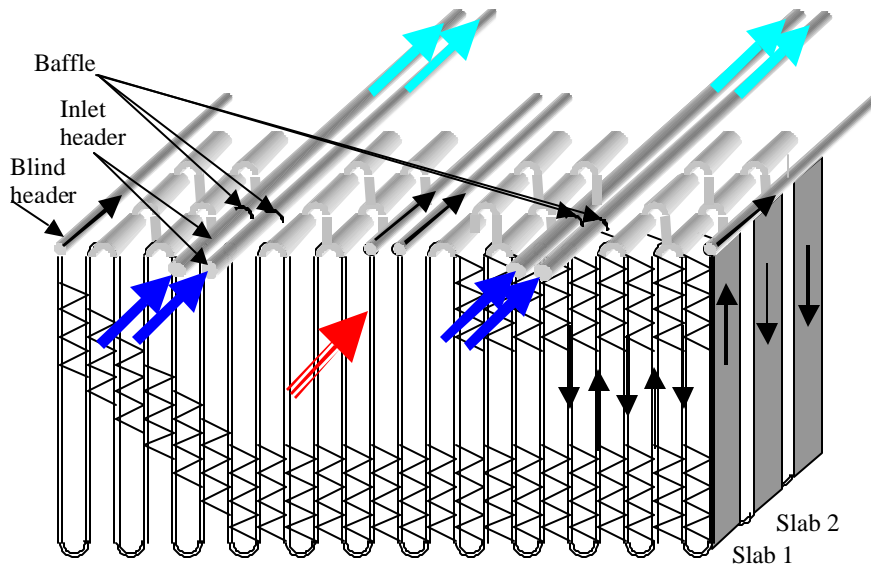


Figure 3.2 Evaporator configuration

3.2 Approach

A detailed model of the heat exchanger is used to calculate refrigerant mass flow rate in each of the four circuits, based on experimental measurements. Key assumptions of the model are:

Airflow is evenly distributed.

The heat exchanger consists of three slabs, however, two of them with the same refrigerant flow direction can be considered one slab to make the computation easier.

Chang & Wang correlation is used to calculate air side heat transfer coefficients.

The refrigerant pressure drop correlation is multiplied a factor to approximate the experimental pressure drop data.

The sequential marching finite volume method is used in the model. To check if it will introduce new numerical error, the model results were compared with those obtained by solving all elements simultaneously using the Newton-Raphson algorithm, and the difference was negligible. So we believe that the sequential marching method will not introduce new numerical error.

3.3 Experimental design

This part focuses on answering the question: what is a good test condition to determine the refrigerant maldistribution problem?

3.3.1 Very large superheated area does not help to determine the distribution

Two tests (Test 1 and Test 2) were carried out with refrigerant exit temperature highly superheated. Table 3.1 shows the experimental data. Test 1 is chosen to analyze.

Table 3.1 Experimental data with refrigerant exit highly superheated

Item		Test 1	Test 2
Air inlet temperature, T_{eai} [°C]		39.72	48.91
Average air outlet temperature (average value at		18.39	32.44
Air flow rate, m_a [kg/s]		0.179	0.228
Refrigerant inlet temperature, T_{eri} [°C]		-3.16	-2.94
Refrigerant inlet quality, x		0.265	0.288
Refrigerant outlet temperature, T_{ero} [°C]	Tero1	9.80	21.04
	Tero2	9.64	18.89
	Tero3	10.36	18.64
	Tero4	9.96	18.63
Refrigerant saturated temperature at outlet		-3.49	-3.23
Refrigerant outlet pressure, P_{ero} [kPa]		3147	3196
Superheat, $? T_{sup}$ [°C], ($T_{ero} - T_{ero_{sat}}$)	? T_{sup1}	13.29	24.27
	? T_{sup2}	13.13	22.12
	? T_{sup3}	13.85	21.87
	? T_{sup4}	13.45	21.86
Refrigerant mass flow rate, m_r [g/s]		19.96	20.43
Cooling capacity, Q [kW]		3.91	3.70

The refrigerant outlet temperatures for our circuits are very close to one another (less than 1°C in Test1). The model is used to find out if it indicates good distribution.

The evaporator is composed of four sub-heat-exchangers as shown in Figure 3.2. One of them is modeled first assuming that the refrigerant distribution is perfect. That is, the inlet quality and inlet pressure are the same as the measured values, and the refrigerant flow rate for each sub-heat-exchanger is $\frac{1}{4}$ of the measured total flow rate.

The model result is shown as in Table 3.2.

Table 3.2 Model result for Test 1

Item	Model result
Air average outlet temperature, T_{eao} [°C]	17.86
Refrigerant outlet temperature, T_{ero} [°C]	11.34
Superheat, $? T_{sup}$ [°C]	14.49
Refrigeration capacity for each sub-HX, Q [kW]	0.977

The calculated refrigerant outlet temperature is 11.34°C when the refrigerant flow rate of each inlet is $0.01996/4=0.00499$ kg/s. Figure 3.3 illustrates the refrigerant and air temperature distribution. The air inlet temperature for the first slab is 39.72 °C, and the air outlet temperature for the first slab is the air inlet temperature for the second slab. One important temperature is the air inlet temperature corresponding to the refrigerant exit, and it is the air outlet temperature for the first slab at the start of the refrigerant flow length. (which is about 11.5°C in this case). It can be seen that the second slab actually rejects heat to the air due to high superheat achieved in the first slab. Because the refrigerant exit temperature cannot get colder than the corresponding air inlet temperature, the

refrigerant exit temperature may not be sensitive to the refrigerant flow rate if it approaches the corresponding air inlet temperature. Figure 3.3 shows that the difference between the two temperatures is very small, and it implies that we cannot use the test result under this test condition to determine if we have a maldistribution problem or not.

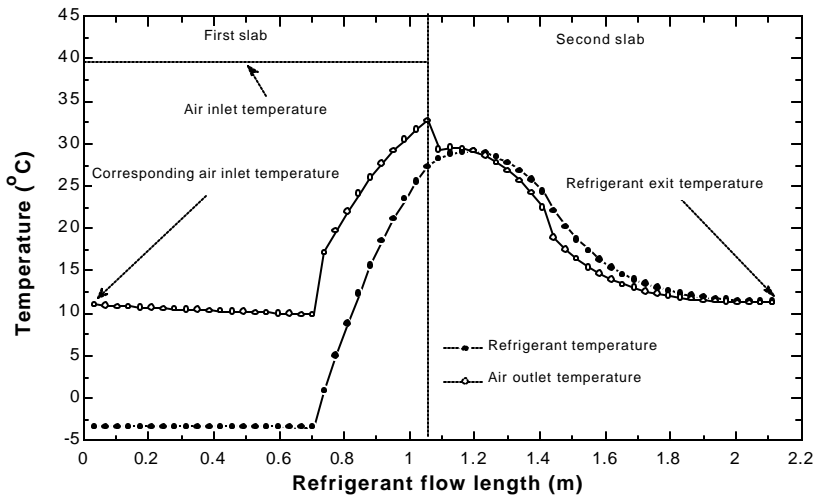


Figure 3.3 Refrigerant and air temperature distribution in Test 1

To illustrate that the refrigerant exit temperature is not sensitive to the change of refrigerant flow rate under this test condition, the refrigerant flow rate for the sub-heat-exchanger is halved while all the other parameters remain unchanged. The model result for this test condition is as shown in Table 3.3.

Table 3.3 Model result for Test1 after reducing the refrigerant flow rate

Item	Model
Air average outlet temperature, T_{eao} [°C]	28.71
Refrigerant outlet temperature, T_{ero} [°C]	12.01
Superheat, ΔT_{sup} [°C]	15.14
Cooling capacity for each sub-HX, Q [kW]	0.492

The model shows that the air outlet temperature is about 10°C higher after reducing the refrigerant flow rate. However, the refrigerant outlet temperature is not sensitive to the change of refrigerant flow rate: it is about 0.7°C higher. Figure 3.4 illustrates the effect of halving the refrigerant flow rate in Test 1.

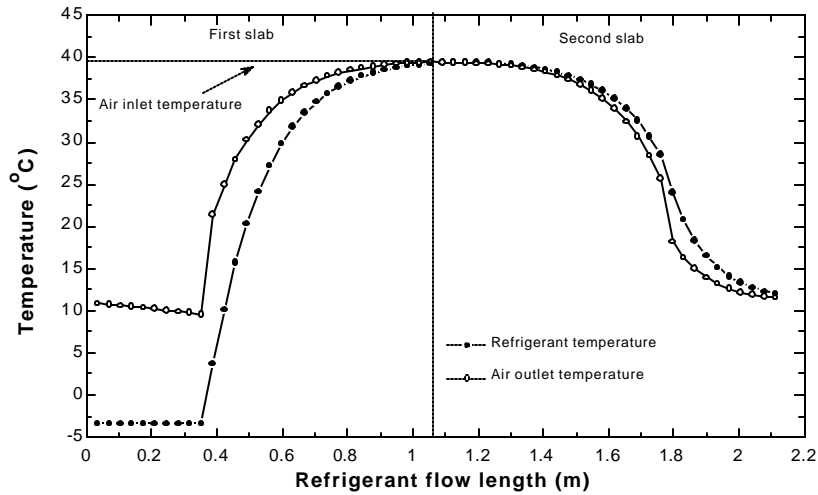


Figure 3.4 Effect of halving the refrigerant flow rate in Test1

From the discussion above, it can be seen that the refrigerant exit temperature is not a good indication of maldistribution when the superheated area is too large. Some other information (e.g. average air outlet temperature, capacity) is needed to determine if the distribution is good or not.

3.3.2 Another kind of bad test condition

Another experiment was conducted with the first slab totally two-phase, so the second slab does not reject heat to the air. However if the heat exchanger effectiveness is high, the refrigerant outlet temperature may approach the corresponding air inlet temperature because the former cannot get warmer than the latter. Again the pinched exit condition makes it difficult to determine the maldistribution.

An example is given below to illustrate this result.

Table 3.4 Example for one bad test condition

Item	Test
Air inlet temperature, T_{eai} [°C]	36
Air flow rate, \dot{m}_a [kg/s]	0.51
Refrigerant inlet temperature, T_{eri} [°C]	1.0
Refrigerant inlet quality, x	0.186
Refrigerant mass flow rate, \dot{m}_r [g/s]	44

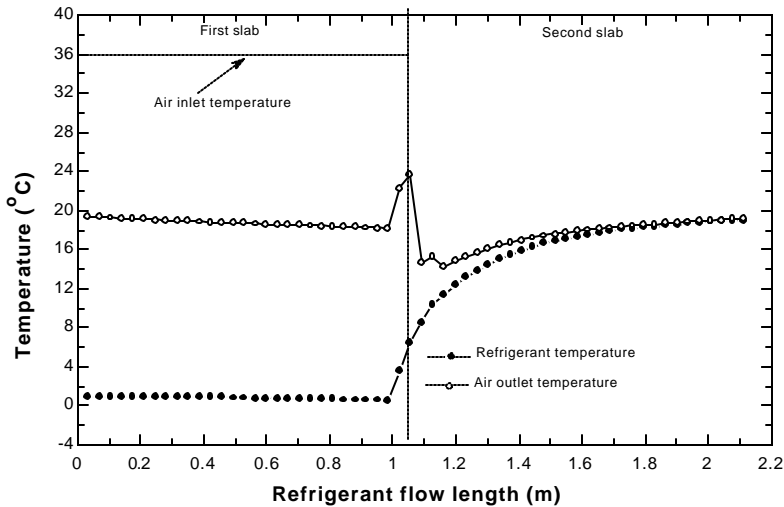


Figure 3.5 Refrigerant and air outlet temperature distribution for the bad test condition

Table 3.4 and Figure 3.5 show one example of this kind of bad test condition. Table 3.4 specifies the test condition and Figure 3.5 shows the refrigerant and air outlet temperature distribution.

3.3.3 Ideal test condition

The ideal test condition is that the first slab is totally two-phase, and the temperature difference between the refrigerant exit and corresponding air inlet is high for the second slab, so the refrigerant exit temperature will be more sensitive to the change of refrigerant flow rate. Increasing the airflow rate, and increasing the air inlet temperature or decreasing the refrigerant inlet temperature can help to obtain this test condition.

Table 3.5 shows one ideal test condition.

Table 3.5 Ideal test condition

Item	Test
Air inlet temperature, T_{eai} [°C]	36
Air flow rate, \dot{m}_a [kg/s]	0.5
Refrigerant inlet temperature, T_{eri} [°C]	1.0
Refrigerant inlet quality, x	0.186
Refrigerant mass flow rate, \dot{m}_r [g/s]	80

Figure 3.6 shows that the refrigerant outlet temperature does not approach closely the corresponding air inlet temperature.

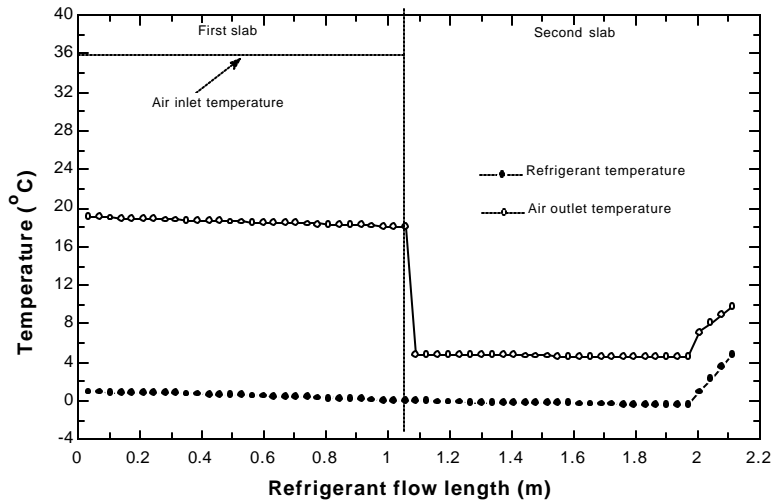


Figure 3.6 Refrigerant and air outlet temperature distribution under ideal test condition

3.4 Results and analysis

3.4.1 Experimental data

Based upon the discussions above, one “good” experimental test was conducted to analyze the refrigerant distribution. Table 3.6 shows the experimental data for this refrigerant distribution test.

Table 3.6 Experimental data for one refrigerant distribution test

Item		Test
Air inlet temperature, T_{ei} [°C]		36.43
Air average outlet temperature (average value at		19.96
Air flow rate, m_a [kg/s]		0.2248
Refrigerant inlet temperature, T_{ei} [°C]		15.65
Refrigerant inlet quality, x		0.186
Refrigerant outlet temperature, T_{eo} [°C]	Tero1	20.75
	Tero2	18.54
	Tero3	19.34
	Tero4	21.07
Refrigerant saturated temperature at outlet		15.49
Refrigerant outlet pressure, P_{eo} [kPa]		5148
Superheat, ? T_{sup} [°C], ($T_{eo} - T_{e_{sat}}$)	? T_{sup1}	5.26
	? T_{sup2}	3.05
	? T_{sup3}	3.85
	? T_{sup4}	5.58
Refrigerant mass flow rate, m_r [g/s]		26.89
Cooling capacity, Q [kW]		3.97

3.4.2 Model results assuming ideal refrigerant distribution

Assuming that the airflow and refrigerant flow is evenly distributed, and the refrigerant inlet pressure and quality for each inlet is the same with the measured value, the model result is shown in Table 3.7.

Table 3.7 Model results assuming ideal distribution condition

Item	Model result
Air average outlet temperature, T_{eao} [°C]	18.37
Refrigerant outlet temperature, T_{ero} [°C]	20.97
Superheat, ΔT_{sup} [°C]	5.32
Cooling capacity for each sub-HX, Q [kW]	1.022

It can be seen from Table 3.7 that the model over predicts the measured capacity about 3%, which might be caused by the refrigerant maldistribution. Figure 3.7 shows the refrigerant temperature and air outlet temperature distribution under this test condition assuming ideal refrigerant distribution.

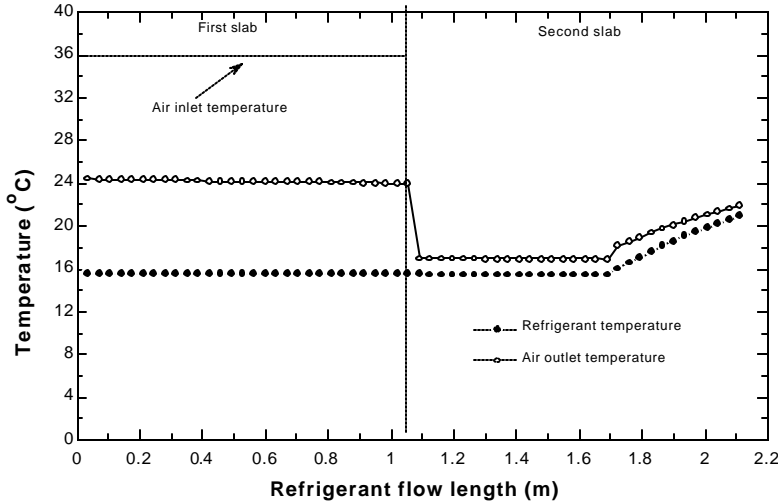


Figure 3.7 Refrigerant and air outlet temperature distribution assuming ideal distribution

3.4.3 Maldistribution analysis

Using the experimental data from Table 3.6, the maldistribution problem is analyzed as follows.

There are four circuits in the system. As it is too complicated to model these four circuits simultaneously, they are divided into two groups. Each group consists of 2 circuits. It is assumed that the distribution between group 1 and group 2 is perfect, that is, maldistribution conditions existing in group 1 is the same as those in group 2. By this simplification, only the flow through two circuits needs to be calculated, and the results of group 1 can be applied to group 2.

The constraint equations for the two circuits are shown as follows. Recall that the mass flow rate in group 1 is half of the total flow rate by the assumption above.

$$mr_1 + mr_2 = \frac{mr}{2} \quad (\text{Mass conservation}) \quad (3.1)$$

$$mr_1 \times x_1 + mr_2 \times x_2 = mr \times x \quad (\text{Vapor conservation}) \quad (3.2)$$

$$Dper_1 = Dper_2 \quad (\text{Same pressure drop}) \quad (3.3)$$

Where mr and x are measured refrigerant flow rate and the inlet quality at the measured refrigerant inlet state.

To illustrate the maldistribution effect on the refrigerant exit temperature, the refrigerant flow rate in circuit 1 is arbitrarily assumed to be 47% of the total flow rate in group 1, that is, 0.00632kg/s. As a result, the mass flow rate in circuit 2 is 0.00713kg/s.

The model result for this refrigerant maldistribution condition is as shown in Table 3.8.

Table 3.8 Model result of maldistribution for circuit 1 and circuit 2

Item	Model	Model
Refrigerant inlet quality, x	0.2478	0.1312
Air average outlet temperature, Teao [°C]	20.02	17.29
Refrigerant outlet temperature, Tero [°C]	23.04	18.12
Superheat, ? Tsup [°C]	7.39	2.47
Cooling capacity for each circuit, Q [kW]	0.9227	1.076

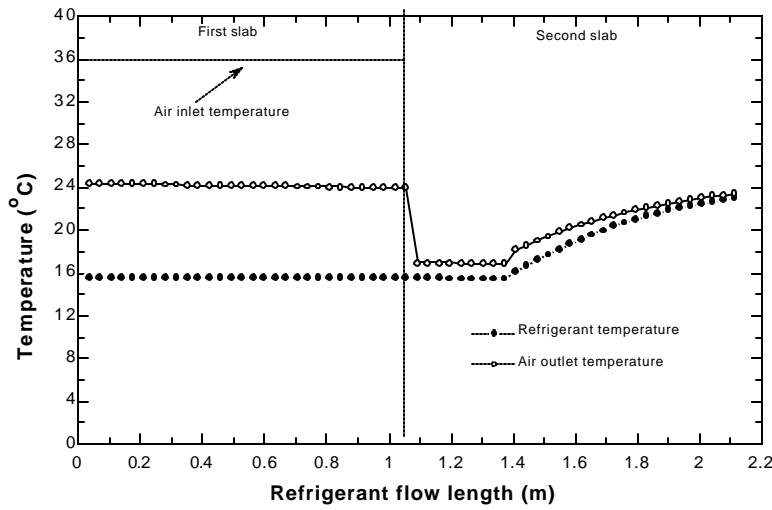


Figure 3.8 Refrigerant and air outlet temperature distribution in circuit 1

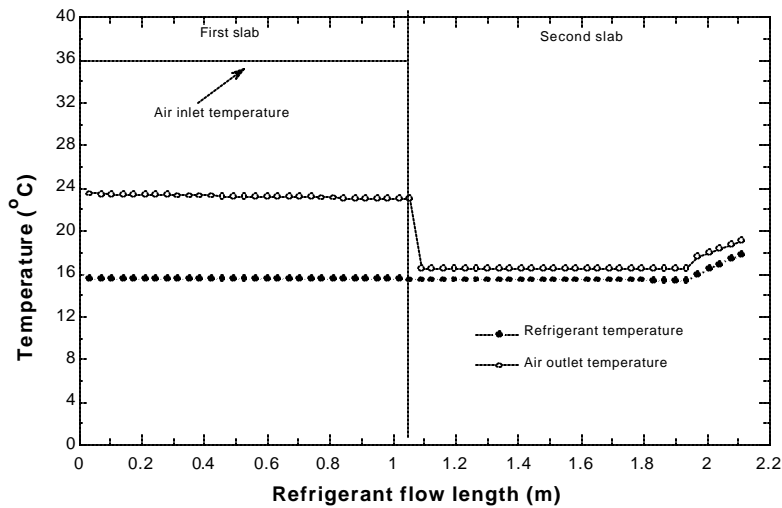


Figure 3.9 Refrigerant and air outlet temperature distribution in circuit 2

Figure 3.8 and 3.9 show that we can tell if the flow is evenly distributed or not by measuring the superheated temperature. The refrigerant exit temperature with higher refrigerant flow rate is lower than that with lower refrigerant flow rate. The calculated refrigerant exit temperature is 23.04 and 18.12 °C respectively in circuit 1 and circuit 2, and the largest lies beyond the range of measured exit temperatures. (Recall that the measured refrigerant exit temperature for each outlet is 20.75, 18.54, 19.34 and 21.07 °C respectively.) These results suggest that the actual refrigerant mass flow distribution between circuit 1 and circuit 2 could be a little better than the 47%/53% assumed here.

The next step is to find out what is the actual refrigerant mass flow distribution based on the experimental data. Given different refrigerant flow rate in circuit 1, the maldistribution effects are shown from Figure 3.10 to 3.14.

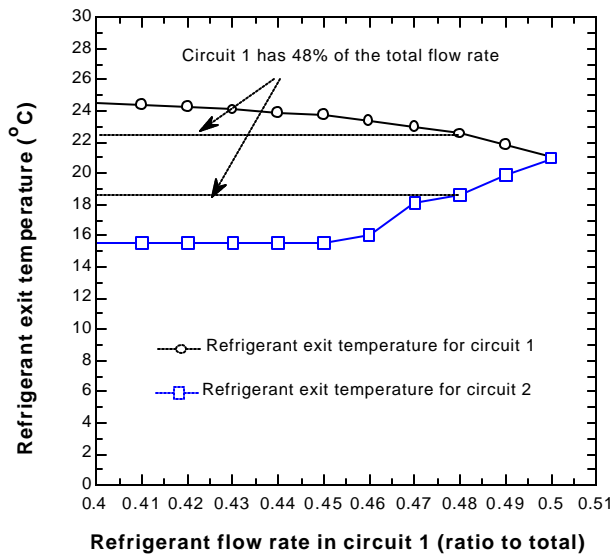


Figure 3.10 Maldistribution effect on refrigerant exit temperature

Figure 3.10 indicates that the severe maldistribution problem can be detected by measuring the range of refrigerant exit temperatures of the four circuits: they are 20.75, 18.54, 19.34 and 21.07 °C. Based on the analysis of these experimental results, we can say that there is no severe maldistribution problem. More quantitatively, when the flow rate in the first circuit accounts for 48% of the total flow rate, the refrigerant exit temperatures for circuit 1 and circuit 2 are about 22 °C and 18 °C respectively which agrees with the experimental data. So the flow rate difference between circuit 1 and circuit 2 is about 5% in our case.

Figure 3.11 shows that the total capacity decreases when maldistribution exists. It drops from 2.044kW to 1.707kW when the refrigerant flow rate for circuit 1 only accounts for 40% of the total refrigerant flow rate. When the refrigerant flow rate for circuit 1 accounts for 48%, which we believe is the actual condition, the loss of capacity is about 3% compared with ideal distribution.

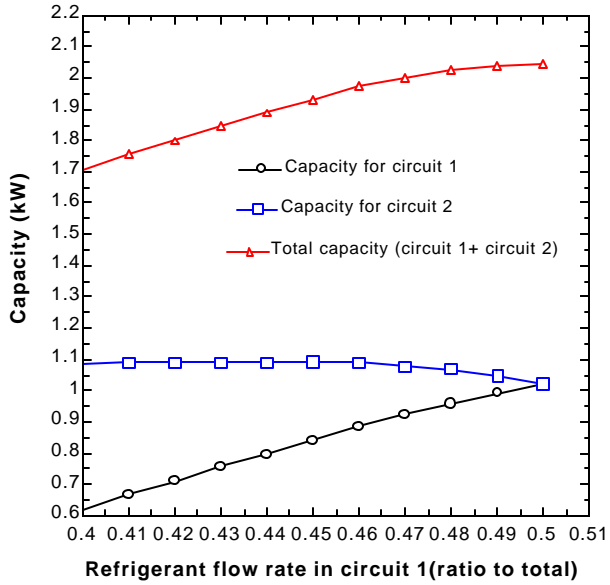


Figure 3.11 Maldistribution effect on capacity

Figure 3.12 shows the maldistribution effect on air outlet temperature. And figure 3.13 shows how the inlet quality increases when the refrigerant flow rate for this circuit decreases. It is somewhat surprising that such a large inlet quality difference between the two circuits still allows 40% of the total refrigerant flow to go through the first circuit.

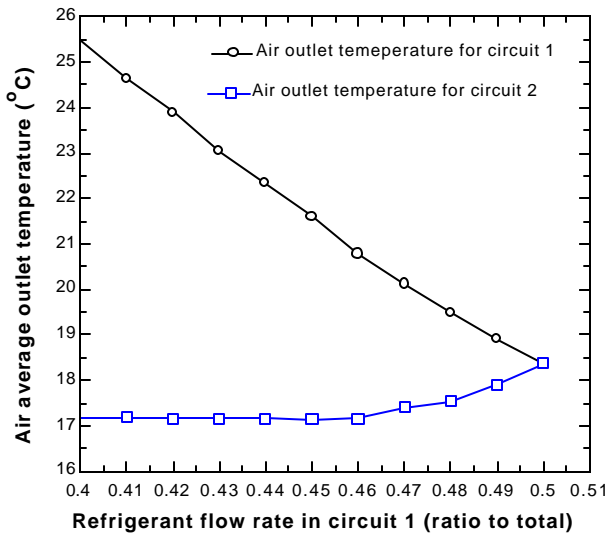


Figure 3.12 Maldistribution effect on air average outlet temperature

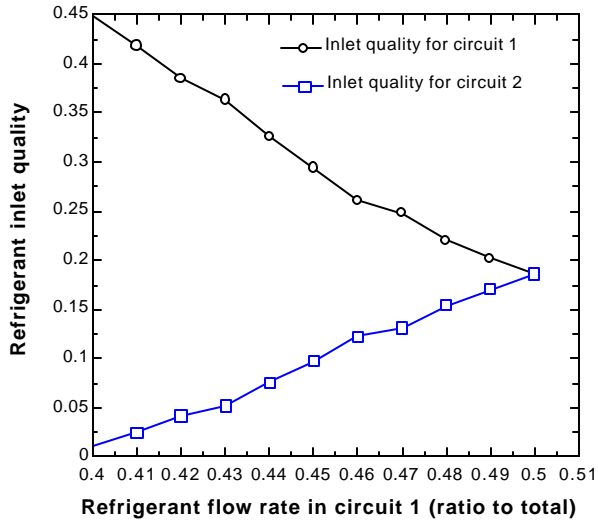


Figure 3.13 Maldistribution effect on refrigerant inlet quality

3.5 Conclusion

Measuring superheat can detect significant maldistribution at certain conditions. Analysis of one such data set for MAC2 indoor heat exchanger suggests that maldistribution may have reduced capacity approximately 3% for this operating condition with 0.19 inlet quality. The corresponding refrigerant mass flow maldistribution for the heat exchanger at this operating condition is about 5%.

Chapter 4 Analysis of the Inclination Angle Experiment

4.1 Introduction

The effect of inlet humidity conditions and inclination angle on the air side thermal hydraulic performance of a brazed aluminum heat exchanger has been investigated experimentally. There are some publications on the effect of inclination angle and inlet humidity conditions on the heat transfer and pressure drop of the heat exchangers. However, most of the published data have considered bare-tube banks, high-fin tube banks and conventional finned tube heat exchangers (Groehn, 1983, Monherit *et al.*, 1986, Moore *et al.*, 1979, Aarde *et al.*, 1993, Chang *et al.*, 1994, Kedzierski, 1997, Mirth *et al.*, 1993, Mirth *et al.*, 1994, Wang *et al.*, 1997, Wang *et al.*, 2000). Mirth *et al.* (1993, 1994) showed that inlet humidity conditions affected the heat exchanger performance. On the other hand, Wang *et al.* (1997, 2000) reported that they did not influence significantly the sensible heat transfer coefficients, while their effect on the pressure drops depended on the heat exchanger configurations, especially the longitudinal tube pitch. When the longitudinal tube pitch was 22 mm, the effect of inlet conditions was negligible, while for the longitudinal pitch of 19.05 mm the friction factors for $RH_1=90\%$ were 5-25% larger than those for $RH_1=50\%$.

A microchannel tube heat exchanger is one of the potential alternatives for replacing the conventional finned tube heat exchangers and has been considered as both evaporator and gas cooler for prototype CO₂ air-conditioning systems (Kim *et al.*, 2000). Many investigators have studied the air side heat transfer and pressure drop characteristics of the louvered fin and flat tube heat exchangers (Sahnoun *et al.*, 1992, Chang *et al.*, 1996, Chang *et al.*, 1997, Kim *et al.*, 2001, Chiou *et al.*, 1994, Kim *et al.*, 2000, McLaughlin *et al.*, 2000, McLaughlin *et al.*, 2000). However, only small amount of published data on the effect of the inclination angle on the performance of the brazed aluminum heat exchangers is available in the open literature. Recently, Osada *et al.* (1999) studied the effect of inclination on the heat transfer and pressure drop characteristics of the louvered fin automotive evaporators with larger flow depth ($Fd=58$ and 70 mm) and conducted condensate visualization tests. They reported that both the leeward and windward inclinations improved heat exchanger performance. Kim *et al.* (2001) investigated the effect of inclination angle ($0^\circ, \pm 30^\circ, \pm 45^\circ$, and $\pm 60^\circ$ clockwise) on the heat transfer and pressure drop of a brazed aluminum heat exchanger with $Fd=20$ mm under dry and wet conditions. They found that the heat transfer performance for both dry and wet conditions was not influenced significantly by the inclination angle ($-60^\circ < \alpha < 60^\circ$), while the pressure drops increased consistently with the inclination angle.

In our residential CO₂ prototype system, the indoor heat exchanger was inclined to 67° off the vertical due to the space limitations in the wind tunnel (Beaver *et al.*, 1999). The effect of inclination in those experiments was not known because the heat exchanger was too large to test at different angles. The purpose of this study is to provide experimental data on the effect of an inclination angle and inlet humidity conditions on the air side thermal hydraulic performance for a smaller brazed aluminum heat exchanger under dry and wet surface conditions. A series of tests are conducted for the air side Reynolds number range of 80-400 with variation of the inclination angles ($0^\circ, 14^\circ, 30^\circ, 45^\circ$ and 67° clockwise) from the vertical position. The pressure drop characteristics are also addressed.

4.2 Experimental set up

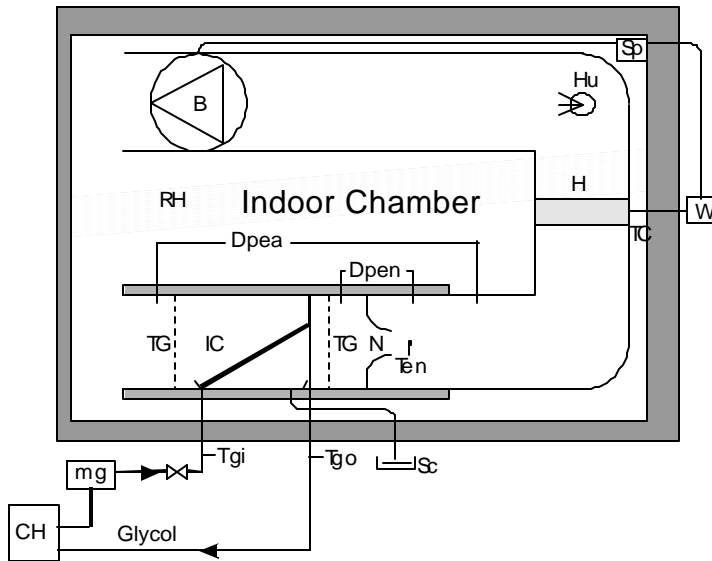
4.2.1 Test heat exchanger

Table 4.1 Geometry of the test heat exchanger

	Items	SI Unit	English Unit
Heat exchanger	Core size: LxHxD	0.394x0.382x0.028 (m)	15.5x15.018x1.1 (in)
	Air-side area, $A_o(A_{fin}+A_{tube})$	4.079 (3.33+0.749) (m ²)	43.901(35.84+8.061) (ft ²)
	Water-side area, A_i	0.749 (m ²)	8.059 (ft ²)
	Water-side hydraulic diameter, $D_{h_{water}}$	2.158 (mm)	0.00708 (ft)
	Air-side hydraulic diameter, $D_{h_{air}}$	3.121 (mm)	0.01024 (ft)
	Tube pitch, T_p	9.855 (mm)	0.388 (in)
Tube	Tube spacing	7.925 (mm)	0.312 (in)
	Tube depth (major axis), T_d	25.4 (mm)	1.0 (in)
	Tube thickness (minor axis)	1.93 (mm)	0.076 (in)
	Wall thickness	0.4064 (mm)	0.016 (in)
	Number of tubes	38	38
	Fin density, FPI	12	12
Fin	Fin height, H	8.28 (mm)	0.326 (in)
	Flow depth, F_d	27.94 (mm)	1.1 (in)
	Fin thickness, δ_f	0.1016 (mm)	0.004 (in)
	Louver pitch, LP	1.397 (mm)	0.055 (in)
	Louver length, LI	6.604 (mm)	0.26 (in)
	Louver angle, La (°)	27	27
	Number of louvers	17	17

4.2.2 Test apparatus

Figure 4.1 shows a schematic diagram of the apparatus used in the study. It consists of a ducted airflow system, heat transfer fluid (glycol) circulation and data acquisition system. It is situated in a constant temperature and humidity chamber that can maintain temperature within $\pm 0.5^\circ\text{C}$ and absolute humidity $\pm 2\%$. The air inlet conditions of the heat exchanger are maintained by controlling the chamber temperature and humidity. The air side pressure drop through the heat exchanger is measured using a differential pressure transducer and the airflow rate is determined from the nozzle pressure difference.



B - Blower, **CH**- Glycol Chiller, **H** – Heater, **Hu** – Humidifier, **IC** – Indoor Coil, **mg** – Glycol Mass Flow Meter, **N** – Nozzle, **Sc** – Condensate Scale, **Sp**– Speed Controller and Tachometer, **TC** – Temperature Controller, **TG** – Thermocouple Grid, **W** – Watt Transducer
 Indices: **a** – air, **e** – evaporator, **g** – glycol, **i** – inlet, **n** – nozzle, **o** – outlet

Figure 4.1 Schematic diagram of test apparatus

The distances between the chamber wall and the wind tunnel inlet, between the wall and one side of the wind tunnel and between the wall and the other side of the wind tunnel are about 1 m, 0.3 m, and 0.6m respectively. The wind tunnel entrance is 1.0 m wide and 0.6m high. The distance between floor and ceiling is about 2.5 m.

4.2.3 Test methods

The heat exchanger is installed in the test section, surrounded by insulation to protect it from heat loss and air leakage. The results depend on the wind tunnel due to contraction and other effects. In the following discussion, the effect of the wind tunnel is ignored.

When the inclination angles were 0° , 14° , 45° and 60° , we tested the evaporator as shown in Figure 4.2. The arrangement is different when the angle is 67°C , shown in Figure 4.3. Because it is somewhat difficult to block the air from the back, we blocked from the front too to avoid air leakage.

One test was conducted to see if the arrangement would affect the test result or not. It turned out that the effect was small. The effect on the calculated air side heat transfer coefficient under dry conditions was less than 3% between the two arrangements. And the effect on the measured pressure drop under dry conditions was less than 5%.

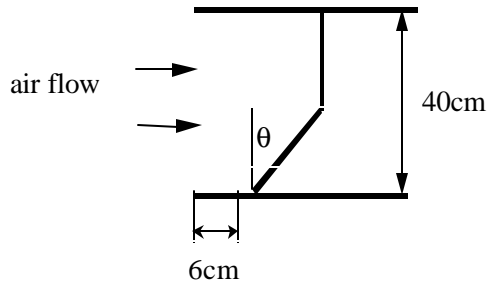


Figure 4.2 Schematic diagram of heat exchanger installation when the inclination angles were 0°, 14°, 45° and 60°

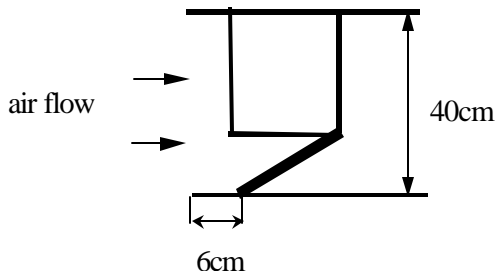


Figure 4.3 Schematic diagram of heat exchanger installation when the inclination angle was 67°

4.3 Experimental Results

The experimental results are shown in this part.

4.3.1 Effect of inclination angle on air side heat transfer

4.3.1.1 Dry surface

4.3.1.1.1 Energy balance agreement Energy balance was measured by three independent methods (Chamber, glycol and air side, one nozzle was covered).

▪ Air side energy balance

$$Q_a = m_a \times h_{a,i} - m_a \times h_{a,o} \quad (4.1)$$

Where,

Q_a air side capacity (kW)

m_a mass flow rate of dry air through evaporator (kg/s)

$h_{a,i}$ enthalpy of air entering evaporator (kJ/kg)

$h_{a,o}$ enthalpy of air entering nozzle (kJ/kg)

Air inlet temperature is measured using an 11X5 thermocouple grid that covers the entire face of duct.

Air inlet dew point is measured through the use of a chilled mirror humidity sensor.

▪ Glycol-side energy balance

$$Q_g = m_g \times (h_{g,o} - h_{g,i}) \quad (4.2)$$

Where,

Q_g glycol-side capacity (kW)

m_g glycol mass flow rate (kg/s)

$h_{g,i}$ enthalpy of inlet glycol (kJ/kg)

$h_{g,o}$ enthalpy of outlet glycol (kJ/kg)

The specific heat of the glycol mixture was determined by Richter, 2000. The concentration of the glycol was determined by measuring the specific gravity of the solution with a hydrometer and the specific heat values can be obtained using *Fluidfile* software from Dow Chemical. A second test was conducted for verification. The test consisted of running just the glycol loop, blower and heater (to maintain a chamber temperature of 70°F). At steady state, the power entering the chamber is equal to the power leaving the chamber. The difference between the heat input (electrical power $\pm 0.5\%$) to and removal from the system (via glycol) was less than 5%. This was within the 7% range of experimental uncertainty. The values for the precision of the measurement were taken to be $\pm 1^\circ\text{C}$ for the thermocouple and 0.5 kg/m^3 for the density (manufacturers spec). The theoretical uncertainty in the specific heat is about $\pm 0.3\%$.

- **Chamber-side Energy Balance**

$$Q_c = W_{el} + Q_{cond} \quad (4.3)$$

$$Q_{cond} = k_f A_f (T_{o,f} - T_{i,f}) + k_c A_c (T_{o,c} - T_{i,c}) + k_w A_w (T_{o,w} - T_{i,w}) \quad (4.4)$$

Where,

Q_c chamber-side capacity (kW)

W_{el} electrical power into chamber (kW)

Q_{cond} heat conduction from environment into chamber (kW)

The chamber was calibrated by placing a heat source within a closed chamber. At steady state, the power entering the chamber in the form of electricity is equal to the amount of heat leaking out of the chamber in the form of conduction through the chamber walls. At least three data points are needed to back out k_f , k_c and k_w for the floor, ceiling and walls, respectively.

- **Temperature calibration**

The temperature difference between two thermocouples at glycol inlet and exit was very small. At equilibrium condition before each series of tests, the difference was about 0.01°C . The temperature difference between two thermocouples at air inlet and exit was about 0.1°C (inlet is higher than exit). These tare values were used to correct all temperature readings.

When a probe is immersed in a flowing fluid, the flow comes to rest in the immediate vicinity of the probe. In this deceleration, kinetic energy is converted into internal energy, which can significantly increase the fluid

temperature. Although this change in temperature is generally small in liquid flows, it can be significant in gas flows. The total and static temperatures of a gas with velocity V and (constant) specific heat Cp are related by the equation

$$T_t = T_{st} + \frac{V^2}{2Cp} \quad (4.5)$$

As a flow is brought to rest at a real probe, the temperature generally is not equal to the total temperature other than in an idealized case or in specially designed probes. Often, as a result of dissipative processes (conduction, viscosity), the temperature is some value less than T_t . The temperature at an adiabatic surface is called the recovery temperature T_r , which is

$$T_r = T_{st} + rT_d \quad (4.6)$$

Where r is the recovery factor, and T_d is the dynamic temperature $T_t - T_{st}$. With a laminar boundary layer flowing along a flat surface parallel to the flow, the recovery factor is equal to the square root of the Prandtl number. In general, the recovery factor around a temperature probe is not uniform and often must be measured if accurate results are required. In our case, the recovery factor is assumed $\sqrt{\text{Pr}}$ (Warren *et al.*, 1998).

Because the air inlet velocity is far less than air velocity in the nozzle, the kinetic energy effect on air inlet temperature is negligible. However it is significant for the air exit temperature measurement when the air velocity is high. For example, the measured air exit temperature is reduced about 0.5°C after it is corrected when the air Reynolds number is about 400. All temperature data presented in this section were first corrected for tare values and kinetic energy.

- **Energy balance result**

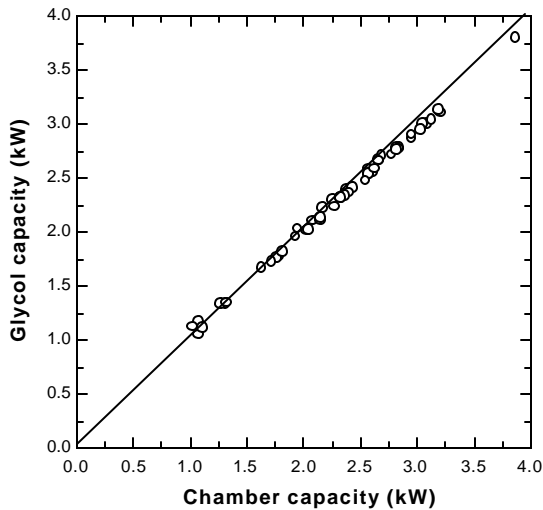


Figure 4.4 Chamber capacity versus glycol capacity under dry condition

From Figure 4.4 we can see that energy balances from chamber and glycol side are close, the difference between the two methods is within 5% when the confidence level is 95%.

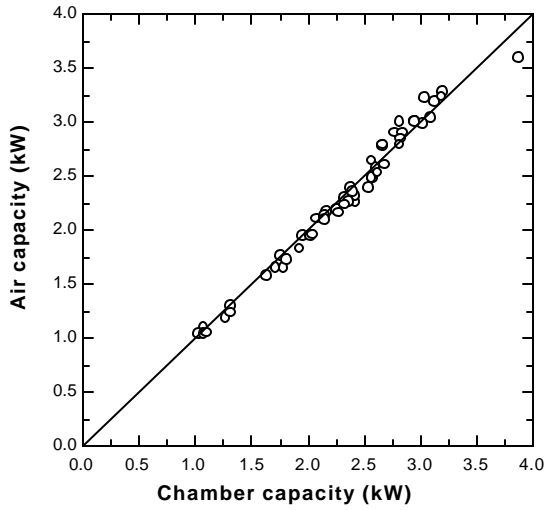


Figure 4.5 Chamber capacity versus air side capacity under dry condition

Figure 4.5 shows that the difference between the energy balances from chamber and air is within 7% when the confidence level is 95%.

▪ **Uncertainty analysis**

In the following discussion, the “Uncertainty Propagation” command in EES is used to calculate how the uncertainties in each of the measured variables propagate into the value of the calculated quantity. The method for determining this uncertainty propagation is described by Taylor, 1994. Assuming the individual measurements (X_1, X_2, \dots) are uncorrelated and random, the uncertainty in the calculated quantity (Y) can be determined as

$$U_Y = \sqrt{\sum_i \left(\frac{\partial Y}{\partial X_i} \right)^2 U_{X_i}^2} \quad (4.7)$$

Where U represents the uncertainty of the variable at the 95% confidence level.

Choose one data point to compare the uncertainties of the three methods.

The heat conduction from environment to chamber is much smaller than the electric power into chamber. The heat conduction counts for less than 10% of the chamber capacity. Due to the accuracy with which the electric inputs to the chamber are measured as well as the ability to accurately measure transmission losses, we believe that chamber calorimetry is the most accurate method to determine capacity. All dry energy inputs are measured with watt transducers within $\pm 2\%$, and five thermocouples on both sides of each wall, floor, and ceiling of the chamber provide temperature differences across the chamber walls within $\pm 0.5^\circ\text{C}$. The uncertainties for the heat conduction, electric input and chamber capacity are 0.170 ± 0.0044 kW, 2.496 ± 0.0493 kW and 2.604 ± 0.0501 kW respectively.

The uncertainty for the glycol capacity is relatively big due to small temperature difference. The glycol flow rate is measured within $\pm 0.2\%$, and the uncertainties for the two thermocouples measuring the glycol inlet and

outlet temperature and for the specific heat of the glycol is $\pm 0.5^\circ\text{C}$, $\pm 0.3\%$ respectively. The calculation for the glycol capacity is $2.559 \pm 1.069\text{kW}$

The uncertainty for the pressure transducer measuring the air pressure drop across the nozzle is $\pm 0.5\%$ and the uncertainty for the two thermocouples measuring the air inlet and outlet temperature is $\pm 0.5^\circ\text{C}$. The calculation for the air side capacity is $2.585 \pm 0.1063\text{kW}$.

So the chamber capacity is used in the following calculation.

4.3.1.1.2 Test conditions

Dry-bulb temperature of the inlet air:	$12 \pm 0.5^\circ\text{C}$
Inlet air velocity:	0.3~4m/s
Inlet glycol temperature:	0~2.5 $^\circ\text{C}$
Glycol velocity inside the tube:	0.4~0.45m/s

4.3.1.1.3 Data reduction

Assume that glycol-side fouling resistance and the wall resistance are negligible. Because the chamber side energy balance is the most accurate one as discussed above, the chamber capacity was used to back out the airflow rate from the air side energy equation.

To see whether or not the refrigerant flow is uniform, the pressure drop along the header and the tube is calculated. Assume that the flow rate is evenly distributed in each tube and the flow rate is assumed half of the total flow rate while calculating the pressure drop along the header.

For laminar flow (ASHRAE Handbook, 1997):

$$f = \frac{64}{\text{Re}} \quad (4.8)$$

$$(H_L)_f = f \left(\frac{L}{D} \right) \left(\frac{V^2}{2g} \right) \quad (4.9)$$

The calculated result shows that the pressure drop along the tube is much higher than that along the header (about 10 times). So it seems that the refrigerant flow is likely to be uniform across the coil.

For the heat transfer coefficients on the glycol side, the Reynolds number based on the hydraulic diameter for glycol is about 110, so it is laminar flow.

The thermal entry length is approximately:

$$\begin{aligned} x_t &= 0.05 \times \text{Re} \times \text{Pr} \times D_h \\ &= 0.05 \times 110 \times 75 \times 0.002138 = 0.88 \text{ m} \end{aligned} \quad (4.10)$$

The hydraulic entry length is:

$$\begin{aligned} x_h &= 0.05 \times \text{Re} \times D_h \\ &= 0.05 \times 110 \times 0.002138 = 0.12 \text{ m} \end{aligned} \quad (4.11)$$

The channel length is about 0.4m; hence flow in the channel is thermally developing, and for most of its length, hydrodynamically developed.

In our case, the duct aspect ratio is about 22, it can be approximated a 2-D duct formed by two wide parallel walls. The mean Nusselt number for parallel plate ducts with equal and uniform temperature on both walls can be computed by the following set of empirical equations proposed by Shah and London, 1984:

$$Nu_{x,T} = \begin{cases} 1.233x^{*-1/3} + 0.4 & \text{for } x^* < 0.001 \\ 7.541 + 6.874(10^3 x^*)^{-0.488} e^{-245x^*} & \text{for } x^* < 0.001 \end{cases} \quad (4.12)$$

$$Nu_{m,T} = \begin{cases} 1.849x^{*-1/3} & \text{for } x^* \leq 0.0005 \\ 1.849x^{*-1/3} + 0.6 & \text{for } 0.0005 < x^* \leq 0.006 \\ 7.541 + 0.0235/x^* & \text{for } x^* > 0.006 \end{cases} \quad (4.13)$$

Where

$$x^* = \frac{x}{D_h \times \text{Re} \times \text{Pr}} \quad (4.14)$$

where x is the tube length.

The surface effectiveness and the fin efficiency are

$$h_{fin} = \frac{\tanh(m \cdot (Fl/2))}{m \cdot (Fl/2)} \quad (4.15)$$

Where Fl is the length of fin.

$$h_{suf} = \frac{A_{tube} + h_{fin} \cdot A_{fin}}{A_{tube} + A_{fin}} \quad (4.16)$$

$$m = \sqrt{\frac{2 \cdot h_a}{k_{fin} \cdot F_{th}}} \quad (4.17)$$

The heat transfer coefficient can be expressed as j factor

$$j = \frac{h_a}{r_m V_c c_p} \text{Pr}^{2/3} \quad (4.18)$$

▪ 1-D finite element, LMTD method

In all the experiments the temperature difference between glycol inlet and outlet is less than 2°C, and the temperature difference between air inlet and glycol inlet is about 10°C. To simplify the calculation we may assume that the glycol temperature is uniform (at its average value) across the coil and it will not cause big error. However, to quantify this error, the evaporator is divided into 20 elements along the glycol flow direction as shown in Figure 4.6. The glycol properties for each element are calculated based on the glycol temperature at the element inlet.

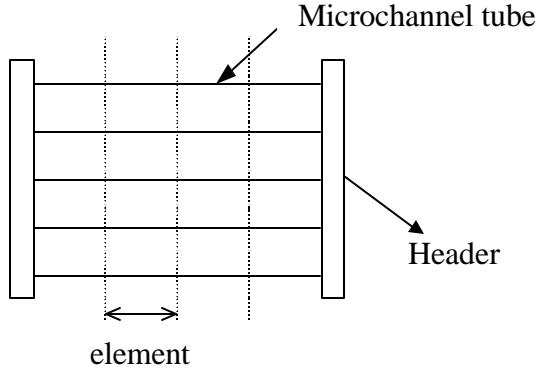


Figure 4.6 Elements along the glycol flow direction

Glycol flow rate, airflow rate, air inlet temperature and heat transfer area are given for each element, and the glycol inlet temperature for the first element is given.

In the calculation of each element, the following equations were used.

$$q = UA \times LMTD \times F \quad (4.19)$$

Because of the small difference between the glycol inlet and outlet temperature, the value of F is nearly 1.

$$\text{Where } LMTD = \frac{(t_{a,i} - t_{g,o}) - (t_{a,o} - t_{g,i})}{\ln\left(\frac{t_{a,i} - t_{g,o}}{t_{a,o} - t_{g,i}}\right)} \quad (4.20)$$

$$\frac{1}{UA} = \frac{1}{h_{suf} h_a A_a} + \frac{1}{h_g A_g} \quad (4.21)$$

$$q = m_a c_{p,a} (t_{a,i} - t_{a,o}) \quad (4.22)$$

$$q = m_g c_{p,g} (t_{g,o} - t_{g,i}) \quad (4.23)$$

The air side heat transfer coefficient can be obtained by setting the sum of q 's to equal the measured chamber side capacity.

Figure 4.7 shows the air side heat transfer coefficients vary with the inclination angle and the Reynolds number based on louver pitch.

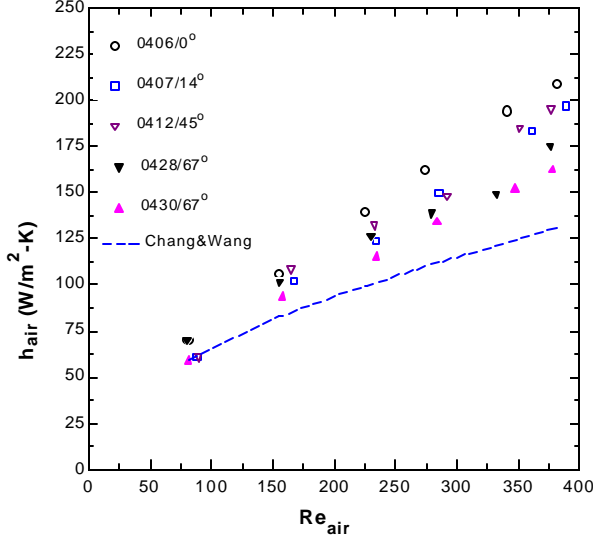


Figure 4.7 Angle effect on h_a under dry condition using 1-D finite element, LMTD method

From Figure 4.7, it seems that the heat transfer coefficients for the dry conditions were not affected significantly by the inclination angles at low Reynolds number. The effect increases as Reynolds number increases. The heat transfer coefficients deteriorated at 67° when the Reynolds number was higher.

The Chang & Wang correlation (Chang et al., 1997) is a generalized heat transfer correlation for this louvered fin geometry. The heat exchanger's geometric parameters and operating conditions were within range that Chang & Wang correlation applies. Figure 4.7 shows that Chang & Wang correlation underestimated air side heat transfer coefficient when Reynolds number is higher than 100. When Reynolds number is about 400, it underestimated h_{air} by 50%.

If we assume that the glycol temperature is uniform across the coil at the average temperature

$$t_{g,ave} = \frac{t_{g,i} + t_{g,o}}{2} \quad (4.24)$$

The glycol properties are calculated based on the glycol average temperature, $t_{g,ave}$. And LMTD method is used on the whole heat exchanger to back out air side heat transfer coefficients

$$Q_{chamber} = UA \times LMTD \times F \quad (4.25)$$

$$\text{Where } LMTD = \frac{(t_{a,i} - t_{g,avg}) - (t_{a,o} - t_{g,avg})}{\ln\left(\frac{t_{a,i} - t_{g,avg}}{t_{a,o} - t_{g,avg}}\right)} \quad (4.26)$$

$$\frac{1}{UA} = \frac{1}{h_{surf} h_a A_a} + \frac{1}{h_g A_g} \quad (4.27)$$

Comparing the calculated results, we can conclude that the error introduced by the uniform glycol temperature assumption is less than 5%.

- **1-D finite element, NTU method**

The effectiveness-NTU method for an unmixed-unmixed cross-flow heat exchanger can also be used in each element to calculate the heat transfer coefficient.

$$\mathbf{e} = \frac{q}{q_{\max}} \quad (4.28)$$

$$q_{\max} = C_{\min} (t_{a,i} - t_{g,i}) \quad (4.29)$$

$$\mathbf{e} = 1 - \exp \left[\left(\frac{1}{C_r} \right) (NTU)^{0.22} \left\{ \exp \left[-C_r (NTU)^{0.78} \right] - 1 \right\} \right] \quad (4.30)$$

$$NTU = \frac{UA}{C_{\min}} \quad (4.31)$$

$$\frac{1}{UA} = \frac{1}{h_{\text{surf}} h_a A_a} + \frac{1}{h_g A_g} \quad (4.32)$$

Theoretically the ϵ calculation is exact only for $C_r=1$. However, it may be used to an excellent approximation for all $0 < C_r \leq 1$, and that is our case.

The difference between the two methods (1-D finite element LMTD and NTU methods) is less than 1%.

- **Uncertainty calculation**

Assume that the uncertainties for the measured parameters are:

$$m_g \pm 0.2\%, t_{g,i} \pm 0.5C, t_{g,o} \pm 0.5C, t_{a,i} \pm 0.5C, t_{a,o} \pm 0.5C, Dp_{e,n} \pm 0.5\%$$

Then the uncertainty of calculated h_a due to instrument errors is about $\pm 10\%$.

To see the effect of the uncertainty in the Nu correlation on the tube-side, assume that the uncertainty in this correlation is $\pm 20\%$. Then the uncertainty of calculated h_{air} increases to $\pm 15\%$.

4.3.1.2 Wet surface

4.3.1.2.1 Energy balance agreement

- **Air side energy balance**

$$Q_a = (m_{a,dry} \times h_{a_i} - m_{a,dry} \times h_{a_o}) - m_w \times h_w \quad (4.33)$$

Where,

$m_{a,dry}$ mass flow rate of dry air through evaporator (kg/s)

m_w mass flow rate of water leaving chamber (kg/s)

h_w enthalpy of water leaving evaporator (kJ/kg)

The condensate is collected in the bottom of the duct and drained out of the chamber. After leaving the chamber, the water is collected in a bucket that hangs from a load cell. In this manner, the weight of the condensate is continually monitored and a value for the mass flow rate of condensate is calculated by fitting a least squared error line to the graph of condensate weight versus time.

The relative humidity at the exit is not measured in the experiment. It is calculated based on the measured condensate rate instead.

The enthalpy of water leaving chamber is evaluated at the glycol inlet temperature. More accurately, evaporator surface temperature should be used. But the difference is negligible.

- **Glycol-side energy balance**

$$Q_g = m_g \times (h_{g,o} - h_{g,i}) \tag{4.34}$$

- **Chamber-side energy balance**

$$Q_c = W_{el} + m_w \times (h_s - h_w) + Q_{cond} \tag{4.35}$$

Where,

m_w mass flow rate of water leaving chamber (kg/s)

h_s enthalpy of steam entering evaporator (kJ/kg)

h_w enthalpy of water leaving chamber (kJ/kg)

- **Energy balance result**

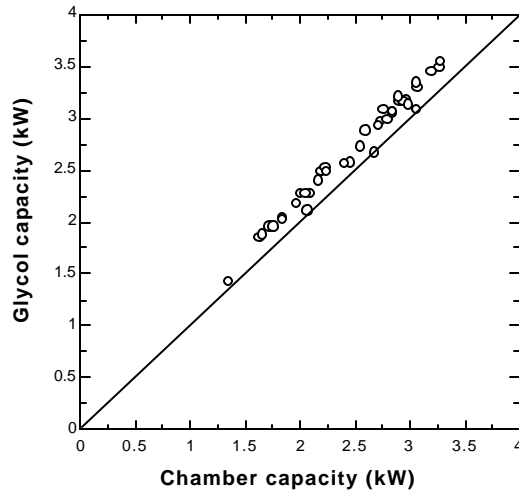


Figure 4.8 Chamber capacity vs. glycol side capacity under wet condition

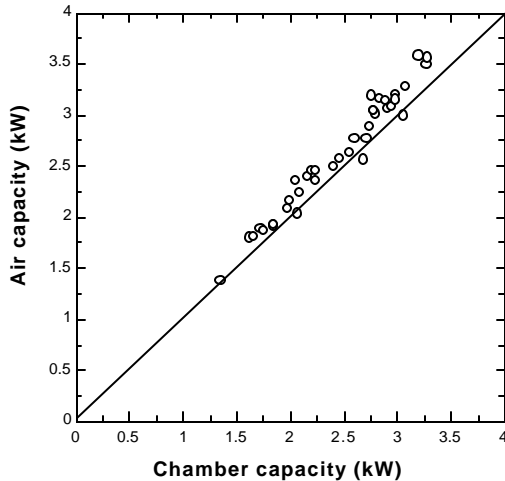


Figure 4.9 Chamber capacity vs. air side capacity under wet condition

From Figure 4.8 and 4.9 it can be seen that chamber side capacity is always lower than glycol and air side capacity. We believe that this is because we lost some condensate in the chamber. We redid some insulation, rotated the steam inlet pipe so that the sparge openings were pointed down, and added a trap inside the steam pipe to collect the water that condensed inside the steam pipe before reaching the air duct. After correcting for this condensate inside the chamber after the experiments were completed, the difference between energy balances dropped from 8% to about 5%. This correction has no effect on the latent heat measurement because the condensate removal rate across the coil remained the same. Condensate spillage outside the test section affected the overall chamber energy balance, but not the latent capacity measurements inside the test section.

Because of the relatively bigger uncertainty of the glycol-side energy balance due to the small glycol temperature changes, and the uncertainty of the lost condensate in the chamber capacity measurement discussed above, the air side energy balance is believed to be the most accurate one. Because it is somewhat difficult to estimate the error of the measured condensate rate, we assume that the error is $\pm 5\%$ to have a rough idea of the uncertainty of air side capacity. The uncertainties for the other measured parameters are the same as those in the dry surface part. The resulting uncertainty of air side capacity is about $\pm 8\%$.

4.3.1.2.2 Test conditions

Dry-bulb temperatures of the inlet air:	$12 \pm 0.5^\circ\text{C}$
Inlet relative humidity for the incoming air:	70% and 80%
Inlet air velocity:	0.3~4m/s
Inlet glycol temperature:	0~2.5°C
Glycol velocity inside the tube:	0.4~0.45m/s

4.3.1.2.3 Data reduction

Assume that glycol-side fouling resistance and the wall resistance are negligible and water film thickness is zero.

- **1-D finite element, LMhD method**

The evaporator is divided into 10 elements along the glycol flow direction as shown in Figure 4.6. The glycol properties for each element are calculated based on the glycol temperature at the element inlet.

Glycol flow rate, airflow rate, air inlet temperature and heat transfer area are given for each element. And glycol inlet temperature for the first element is given.

In the calculation of each element, the following equations were used.

$$q = U_{o,w} A_o LMhD \quad (4.36)$$

$$\text{Where } LMhD = \frac{(h_{a,i} - h_{s,g,i}) - (h_{a,o} - h_{s,g,o})}{\ln \left(\frac{h_{a,i} - h_{s,g,i}}{h_{a,o} - h_{s,g,o}} \right)} \quad (4.37)$$

$$q = m_a (h_{a,i} - h_{a,o}) \quad (4.38)$$

$$q = m_g c_{p,g} (t_{g,o} - t_{g,i}) \quad (4.39)$$

The air side heat transfer coefficient can be obtained by setting the sum of q 's to equal the measured air side capacity.

The uncertainty of the calculated sensible heat transfer coefficients due to measurement errors is about $\pm 20\%$.

- **1-D finite element, NTU method**

The evaporator is divided into 10 elements along the glycol flow direction as shown in Figure 4.6. And NTU method is used to calculate air side heat transfer coefficient.

In the calculation of each element, the following equations were used.

$$NTU = \frac{U_{o,w} A_o}{m_a} \quad (4.40)$$

$$q_{\max} = m_a (h_{a,i} - h_{s,g}) \quad (4.41)$$

$$q = e q_{\max} \quad (4.42)$$

$$e = 1 - \exp(-NTU) \quad (4.43)$$

The air side heat transfer coefficient can be obtained by setting the sum of q 's to equal the measured air side capacity.

The uncertainty of the calculated sensible heat transfer coefficients due to measurement errors is about $\pm 20\%$.

The derivation and assumptions of LMhD and NTU methods are discussed in Chapter 2. The difference of the calculation result between LMhD and NTU method is less than 0.5% for all the data points.

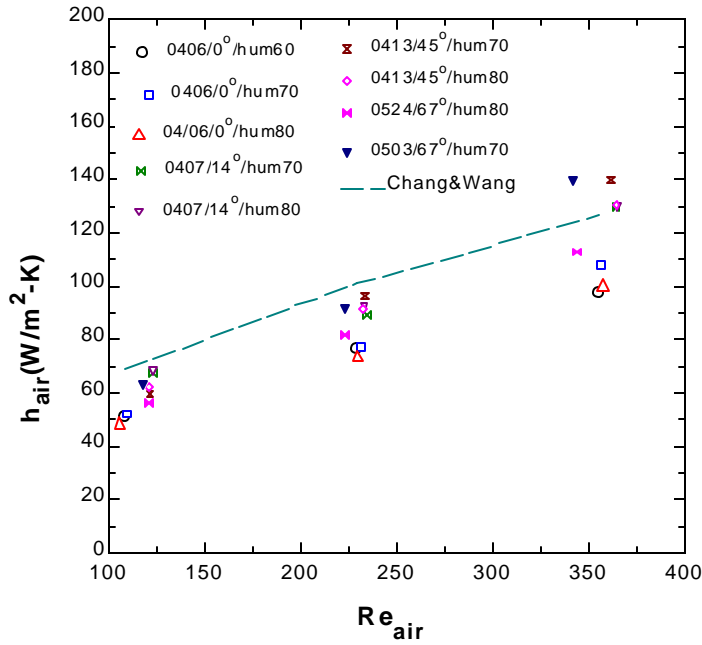


Figure 4.10 Angle effect on air side heat transfer coefficient under wet surface condition using 1-D finite element, NTU method

Figure 4.10 shows that the sensible heat transfer coefficients were close at 14° and 45°, deteriorated at 0° due to drainage problem to be discussed later.

▪ **1-D finite element, separation of sensible and latent heat method**

The LMhD and NTU methods discussed above do not separate the sensible and latent heat. The method discussed in this part calculates sensible and latent heat separately. And it needs to calculate the surface temperature explicitly.

It was shown before that the assumption of uniform glycol temperature would not cause big error. To simplify the calculation, the glycol temperature is assumed uniform across the coil at the average glycol temperature. To take the effect of surface temperature variation along the evaporator depth into consideration, the evaporator is divided into 20 elements along the evaporator depth as shown in Figure 4.11.

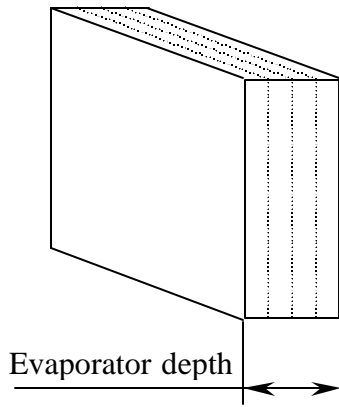


Figure 4.11 Element number along the depth of the heat exchanger

In the calculation of each element, the following equations were used.

Heat transfer between glycol and surface

$$q = h_g A_g (t_p - t_{g,avg}) \quad (4.44)$$

Sensible heat transfer between surface and air

$$q_s = h_a h_o A_a \left(\frac{t_{a,i} + t_{a,o}}{2} - t_p \right) \quad (4.45)$$

Latent heat transfer between surface and air

$$q_l = h_D A_a h_o \left(\frac{w_{a,i} + w_{a,o}}{2} - w_p \right) h_{fg} \quad (4.46)$$

$$q_s = m_a c_{p,a} (t_{a,i} - t_{a,o}) \quad (4.47)$$

$$q_l = DG_s (h_s - h_w) \quad (4.48)$$

$$DG_s = m_a (w_{a,i} - w_{a,o}) \quad (4.49)$$

The air side heat transfer coefficient can be obtained by setting the sum of q 's to equal the measured air side capacity.

The uncertainty of the calculated sensible heat transfer coefficients due to measurement errors is about $\pm 20\%$.

Figure 4.12 shows the calculation results and we can see that the difference of calculated air side heat transfer coefficients between this method and NTU method discussed above is less than 5% for all the data points, apparently due to computational assumptions (uniform glycol temperature) and analytical assumptions required to derive the log mean enthalpy relationship (linear relationship between the saturated temperature and enthalpy, ignored small term, evaluation of b).

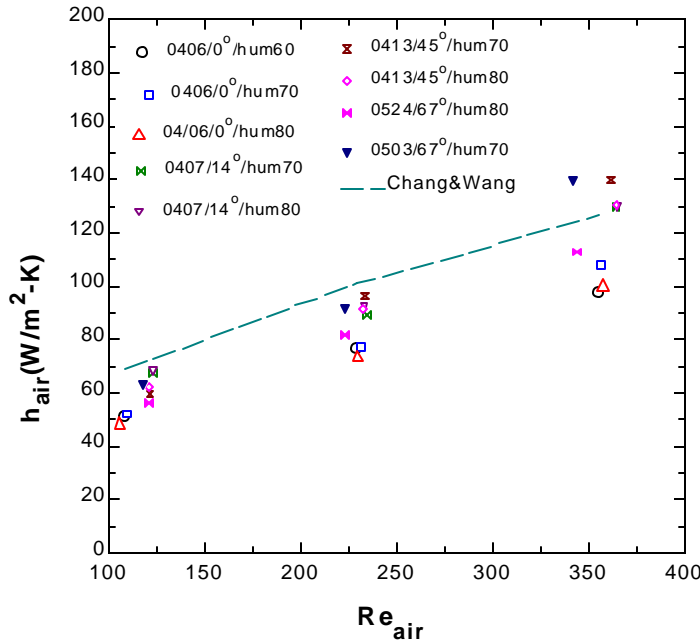


Figure 4.12 Angle effect on air side heat transfer coefficient under wet surface condition using separation of sensible and latent heat method

Recall that we only use the total heat transfer rate to back out air side heat transfer coefficients for all three methods discussed above, and the results are close. However, we also measured the sensible and latent heat transfer during experiments. In separation of sensible and latent heat method, sensible heat and latent heat are calculated at the same time as backing out air side heat transfer coefficients. Now, the question is whether or not we can predict the sensible and latent heat well.

Given the uncertainties of the sensible heat transfer coefficients and the measured parameters, the uncertainty of the calculated sensible heat is about $\pm 12\%$ and the uncertainty of the calculated latent heat is about $\pm 20\%$ at the 95% confidence level.

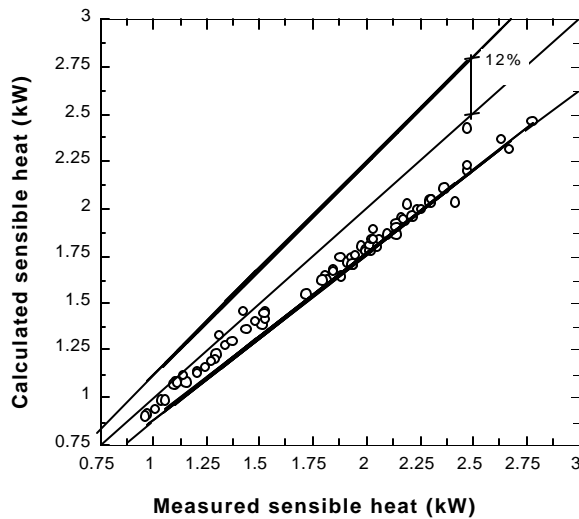


Figure 4.13 Calculated vs. measured sensible heat

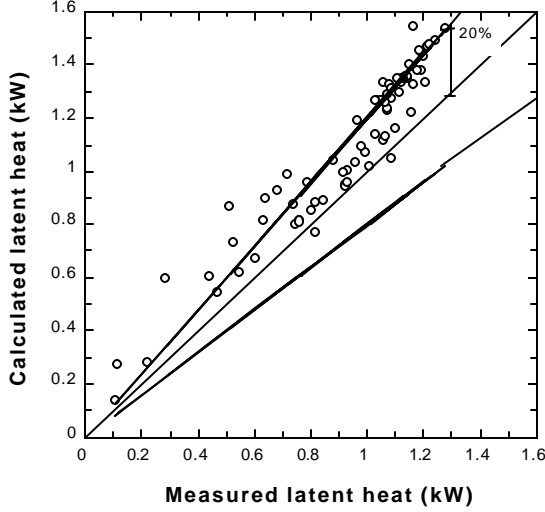


Figure 4.14 Calculated vs. measured sensible heat

Figure 4.13 and 4.14 show that we always over predict the sensible heat and under predict the latent heat. However, about 90% of the calculation results are within the experimental error.

By comparing the calculated air side heat transfer coefficients under dry and wet surface conditions, we can see that the calculated air side heat transfer coefficients under wet surface conditions are much lower than those under dry surface conditions when the Reynolds number is higher than 200.

4.3.1.2.4 Discussion

- **Evaporation effect on condensate measurement**

The evaporation occurring from the floor of the wind tunnel may adversely affect the condensate measurement. A rough calculation was done to see if it is a significant factor. Assume that the floor is a wet flat plate (Frank et al., 1996).

$$n_A = \bar{h}_m A_s (\mathbf{r}_{A,s} - \mathbf{r}_{A,\infty}) \quad (4.50)$$

The calculated air exit relative humidity is about 95% based on the condensate rate measurement, so it can be expected that the evaporation amount is very small.

Assume that the air velocity is 0.5m/s, the floor area is 0.5m², the characteristic length is 1m, the air exit temperature is 10°C, and the floor temperature is the same as the air exit temperature.

$$\text{Re}_L = \frac{u_\infty L}{\nu} = \frac{0.5 \times 1}{15 \times 10^{-6}} = 0.3 \times 10^5 \quad (4.51)$$

$$\overline{Sh}_L = 0.664 \text{Re}_L^{1/2} Sc^{1/3} = 0.664 \times (0.3 \times 10^5)^{1/2} \times 0.6^{1/3} = 97 \quad (4.52)$$

$$\bar{h}_m = \overline{Sh}_L \left(\frac{D_{AB}}{L} \right) = 97 \times \frac{2.6 \times 10^{-5}}{1} = 2.5 \times 10^{-3} \text{ m/s} \quad (4.53)$$

$$n_A = \bar{h}_m A_s [\mathbf{r}_{A,s}(T_s) - \mathbf{f}_\infty \mathbf{r}_{A,s}(T_\infty)]$$

$$= 2.5 \times 10^{-3} \times 0.5 \times 0.0077 \times (1 - 0.95) = 4.8 \times 10^{-7} \text{ g / s} \quad (4.54)$$

And it is negligible compared with the measured condensate rate, which is roughly 0.5g/s.

▪ **Water drainage effect**

Under wet-coil conditions, data were not repeatable when the coil was vertical. We recently concluded, tentatively at least, that a modest angle of attack promotes drainage. Probably that is why the auto industry routinely tilts its evaporators about 10 degrees off the vertical. Apparently it is also beneficial for the thin (16mm) coils used in our residential prototype. We also believe that the louvers in microchannel heat exchangers can become bridged with condensate under some conditions (e.g. at low face velocities in vertical orientation), so it appears as a flat fin and has degraded performance. Surprisingly, they remain bridged as airflow rate is increased. However, if the airflow is initially large and the coil then begins to condense moisture, the drainage appears to be unimpaired.

To see the water drainage effect on air side pressure drop and heat transfer coefficient, we ran some tests at 0° angle attack, 80% humidity, and 900cfm (Re_{air} is about 350). The results were not repeatable, but a systematic relationship was observed.

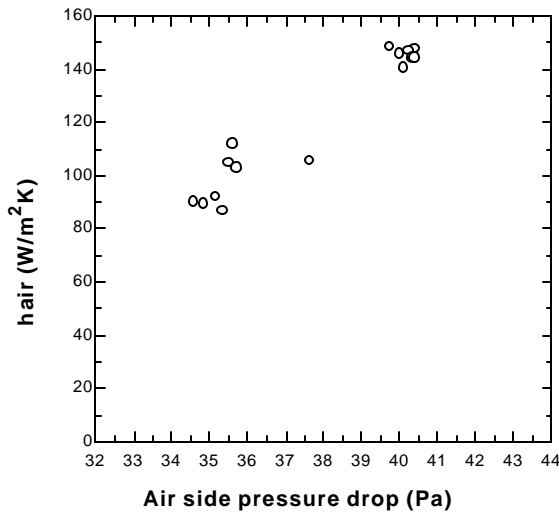


Figure 4.15 Water draining effect

Figure 4.15 shows that the air side heat transfer coefficients increase with the air side pressure drop, perhaps due to condensate bridging between fins. Upon close inspection of the experimental procedures, it was found that the high air pressure drop and air-side heat transfer coefficient occurred when the evaporator was initially dry and the 900 cfm test was run before any lower air flow tests. It indicates that the condensate bridging between fins will not happen if there is no bridging initially and the air flow rate is high enough. The low air pressure drop and airside heat transfer coefficient happened when the 900 cfm experiment was ran after some lower air flow rate experiments under wet surface conditions. It suggests that there is bridging between fins when the air flow rate is low. And surprisingly, the bridging still persists as the air flow rate is increased gradually to 900 cfm.

4.3.2 Effect of inclination angle on air side pressure drop

The pressure drops for dry conditions were measured with isothermal conditions (Only the blower was run without feeding refrigerant), and compared to experiments at wet conditions the pressure drops were measured for inlet humidities between 60-90%.

Figure 4.16 shows how air side pressure drop varied with face velocity and inclination angle. As expected, pressure drops for both dry and wet conditions increase systematically with face velocity and inclination angle. The pressure drops for wet conditions are 3-14 % larger than those for dry conditions at the same face velocity. For $\theta = 67^\circ$ a significant pressure drop increase was occurred. This result is similar to that by Kim *et al.* (2000), who reported pressure drops increased significantly when θ is 60° . Furthermore, in case of $\theta = 67^\circ$, there is an upstream duct which will causes the additional upstream losses associated with oblique air entrance to the heat exchanger

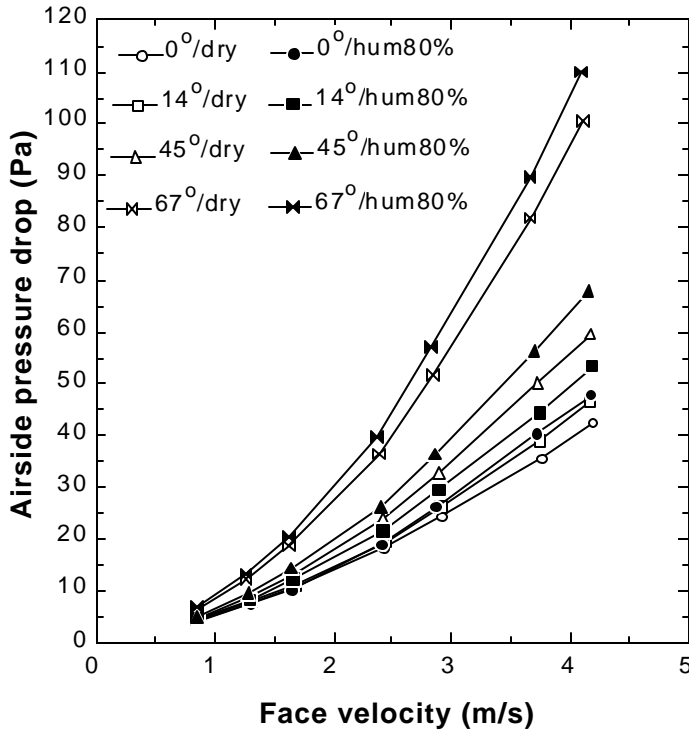


Figure 4.16 Angle effect on air side pressure drop

The pressure drop can be expressed using f factors

$$f = \frac{A_c}{A_o} \frac{r_m}{r_1} \left[\frac{2r_1 \Delta P}{(r_m V_c)^2} - (K_c + 1 - s^2) - 2 \left(\frac{r_1}{r_2} - 1 \right) + (1 - s^2 - K_e) \frac{r_1}{r_2} \right] \quad (4.55)$$

where K_c and K_e are coefficients for pressure loss at the inlet and outlet of the heat exchanger (Kays *et al.*, 1984).

Figure 4.17 shows the relationship between the louvers and the airflow direction. In the worst case of 67° angle of attack, the flow must turn 67° to enter the channels between the fins, and then turn an additional 27° to become louver-directed. The shortfall in j factor at the highest inclination angle suggests that the ideal of louver-directed flow is not achieved. Surprisingly, the data at lower inclination angle ($\theta < 45^\circ$) show little degradation in

heat transfer, suggesting that the flow remains generally louver-directed. The pressure drop penalty is apparent from Figure 4.16, and increases monotonically with turning angle.

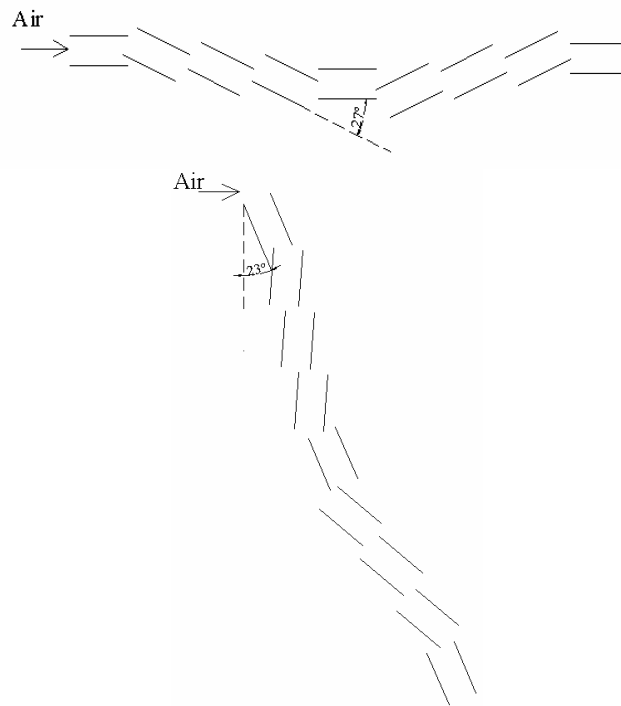


Figure 4.17 Relationship between the louvers and the airflow direction

Figure 4.18 shows the effect of air inlet humidity on the pressure drops. The inlet humidity does not influence significantly pressure drops, similar to that for the conventional finned round tube heat exchangers with fully wet surface (Wang *et al.*, 1997). On the other hand, the previous test data with the micro-channel heat exchanger with smaller fin and louver pitch ratio ($F_p / L_p = 1.4/1.7$) and larger flow depth ($F_d = 41.8$ mm) showed that the air inlet humidity affected systematically the air side pressure drops (Boewe *et al.*, 1999). This difference probably is due to the difference of heat exchanger geometry. The heat exchanger tested in this study has larger fin and louver pitch ratio ($F_p / L_p = 2.1/1.4$) and smaller flow depth ($F_d = 27.9$ mm), and so the effect of condensate amount on the surface may be smaller compared to the heat exchanger with smaller fin pitch and larger flow depth, suggesting the inlet humidity effect on the pressure drops depends on heat exchanger configuration, especially fin pitch.

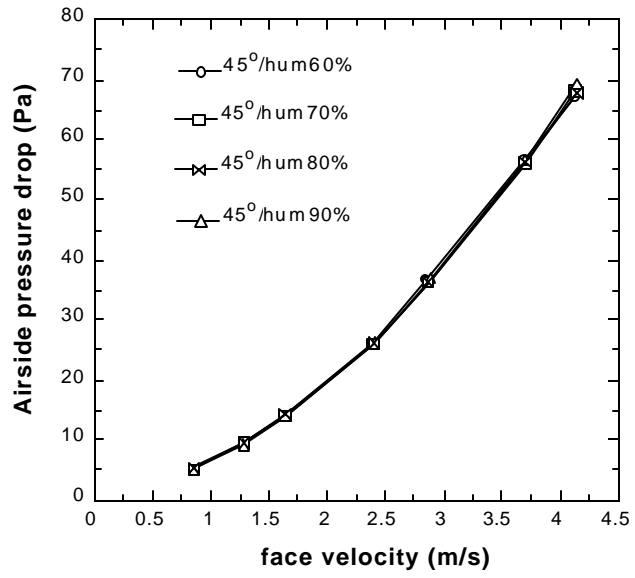


Figure 4.18 Inlet humidity effect on the air side pressure drop

Chapter 5 Frost Deposition and Refrigerant Distribution in Microchannel Heat Exchangers

5.1 Introduction

As part of comprehensive experimental program in transcritical R744 system and component research, Beaver *et al.* (1999a) and Richter *et al.* (2000) showed that the performance of the R744 residential heat pump system was better in most cases than a baseline R410A system. This paper deals with a problem that was identified *a posteriori* in an outdoor coil that had some flow distribution problems that significantly degraded its performance. The experimental data showed that outdoor coil (evaporator) performance plays an important role in determining the cycle COP for one of the first heat pump prototypes to use flat multiport (microchannel) tubes. Therefore a closer investigation of refrigerant maldistribution patterns was warranted. Microchannel condensers have dominated the automotive a/c market by maximizing performance for a fixed size and weight, but must operate as evaporators if they are to be used in heat pumps. That application introduces two major difficulties: refrigerant distribution and frosting/defrosting operation.

Distribution problems in feeding microchannel evaporators can be caused by the non-homogeneity of the entering two-phase refrigerant. Such maldistribution reduces effectiveness of the evaporator, produces an uneven exit air temperature profile, and sometimes uneven frosting of the evaporator surface. Generally these problems can be broken down into two categories that do not necessarily show up independently. The first type is maldistribution along the length of the header or among the microchannel tubes. Another distribution problem occurs among the different ports within a single microchannel tube, which is more difficult to characterize, as the effects will be masked by the high thermal conductivity of the aluminum heat exchanger.

Better understanding of two-phase flow characteristics in the header region is an important issue for full heat exchanger performance. A number of investigations have been performed on two-phase flow distribution. Choi *et al.*, (1993) and Kim *et al.*, (1995) studied the effect of header shape on flow distribution. Rong *et al.*, (1995) discussed the effects of header orientation. Watanabe *et al.*, (1995) and Kariyasaki *et al.*, (1995) investigated two-phase flow in a multi-pass tube setup experimentally to elucidate the effect on the flow distribution of mass flux, quality at the header inlet and number of passes. However, most of previous works are focused on fully developed two-phase flow. Flow characteristics in the actual headers still remain largely unknown and few flow distribution studies have been reported yet for microchannel heat exchangers with vertical headers. The experimental results reported here describe flow distribution in microchannel heat exchangers with vertical headers.

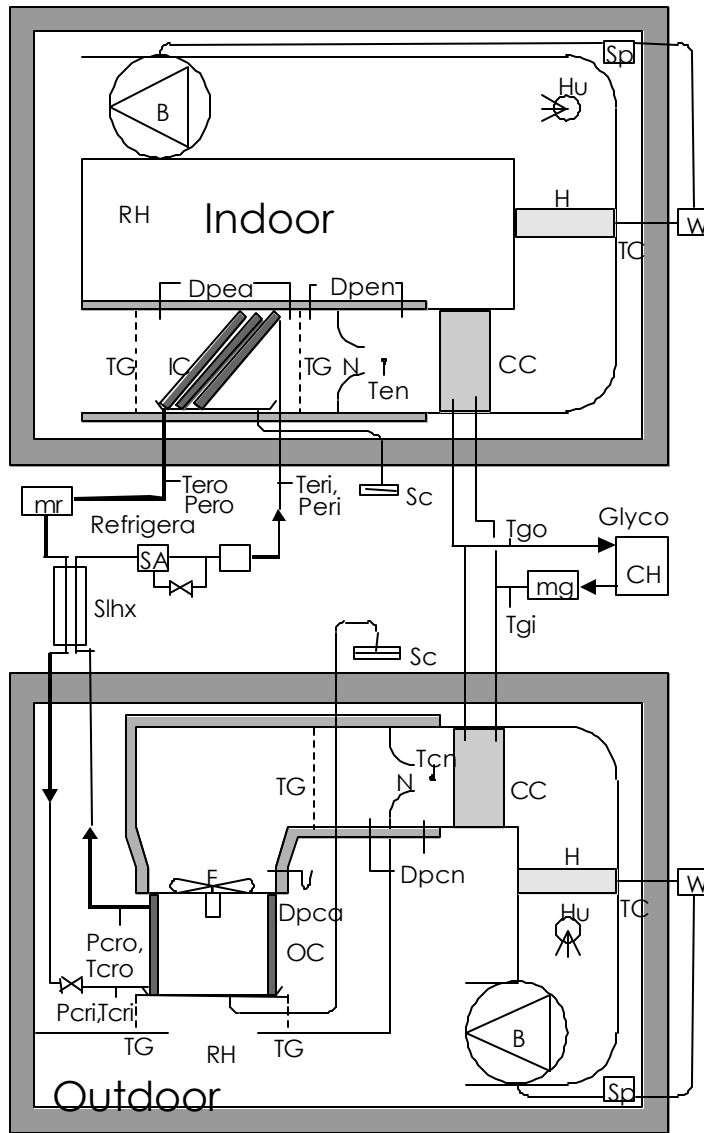
Water (vapor) is a convenient and inexpensive tracer gas for identifying distribution problems by observing frost deposition patterns. The idea is that if there exists severe maldistribution problem in the header, tubes with either a higher entering quality or a lower mass flow rate may contain refrigerant that enters the superheat region earlier. The rapid rise in refrigerant temperature would then lead to an increase in surface temperature, and little or no frost would accumulate on regions with superheated vapor. This type of refrigerant maldistribution can be detected indirectly, by observing the unevenness of frosting. It is difficult to measure variations in frost thickness, but relatively simple to identify photographically those areas where the surface temperature approaches and then exceeds the dew point of the entering air (e.g. where superheated vapor exists). Although the magnitude of the

refrigerant maldistribution is masked by the high thermal conductivity of the aluminum heat exchanger, it is a good qualitative indicator of the extent of maldistribution, which can help us to understand the flow distribution in the header.

5.2 Experimental facilities

Separate environmental chambers containing wind tunnels have been constructed for each heat exchanger. The test facilities are described in detail by Beaver *et al.* (1999a). A schematic of the test facility is given in Figure 5.1.

The facility consists of two environmental chambers that can maintain outdoor and indoor temperature within $\pm 0.5^\circ\text{C}$ and absolute humidity $\pm 2\%$. A variable speed wind tunnel in each chamber simulates the range of operating conditions encountered in real applications, and allows measurement of air-flow rates within $\pm 1\%$. Coriolis type mass flow meters together with immersion thermocouples and electronic pressure transducers both upstream and downstream of every component yield refrigerant-side capacity determinations repeatable within $\pm 1\%$. Room calorimetry is the most accurate: the walls are made of 30 cm thick polyurethane with five thermocouples on both sides of wall, floor, and ceiling of each environmental chamber. Heat losses are carefully calibrated so that error is within $\pm 0.1\%$ of the total system capacity (10 kW). All dry energy inputs (electric) are measured within $\pm 0.2\%$. The test results show agreement between the independently determined capacities to be within $\pm 3\%$, with the error due primarily to uncertainties in air side calorimetry.



B – Blower, **C** – Compressor, **CC** – Cooling Coil, **CH** – Glycol Chiller, **Dp** – Differential Pressure Transducer, **F** – Fan, **H** – Heater, **Hu** – Humidifier, **IC** – Residential Indoor Coil, **mg** – Glycol Mass Flow Meter, **mr** – Refrigerant Mass Flow Meter, **Mtr** – Motor, **N** – Nozzle, **OC** – Residential Outdoor Coil, **P** – Pressure Transducer, **RH** – Relative Humidity Probe, **S** – Separator, **SA** – Suction Accumulator, **Sc** – Condensate Scale, **Slhx** – Suction Line Heat Exchanger, **Sp** – Speed Controller and Tachometer, **T** – Thermocouple, **TC** – Temperature Controller, **TG** – Thermocouple Grid, **W** – Watt Transducer, **XV** – Metering Expansion Valve
 Indices: **a** – air, **c** – condenser, **cp** – compressor, **e** – evaporator, **g** – glycol, **i** – inlet, **n** – nozzle, **o** – outlet, **r** – refrigerant, **sh** – suction line heat exchanger

Figure 5.1 Test facilities for R744 prototype residential split system

The R744 system uses a prototype semi-hermetic reciprocating compressor manufactured by Dorin. The compressor motor is rated at 3 kW at 380V/50 Hz, and the displacement of the compressor is rated at 2.7 m³/h at 1450 rpm. The R744 compressor is controlled by a variable frequency drive so that the capacity can be adjusted.

5.3 Heat exchanger

The heat exchangers in the R744 system were designed to match the geometry of the baseline R410A a/c-only system as closely as practical. As a result, they were not designed to fully capitalize on the properties of R744, nor were they designed for reversible (heating mode) operation. Figure 5.2 shows picture of the R744 outdoor unit.

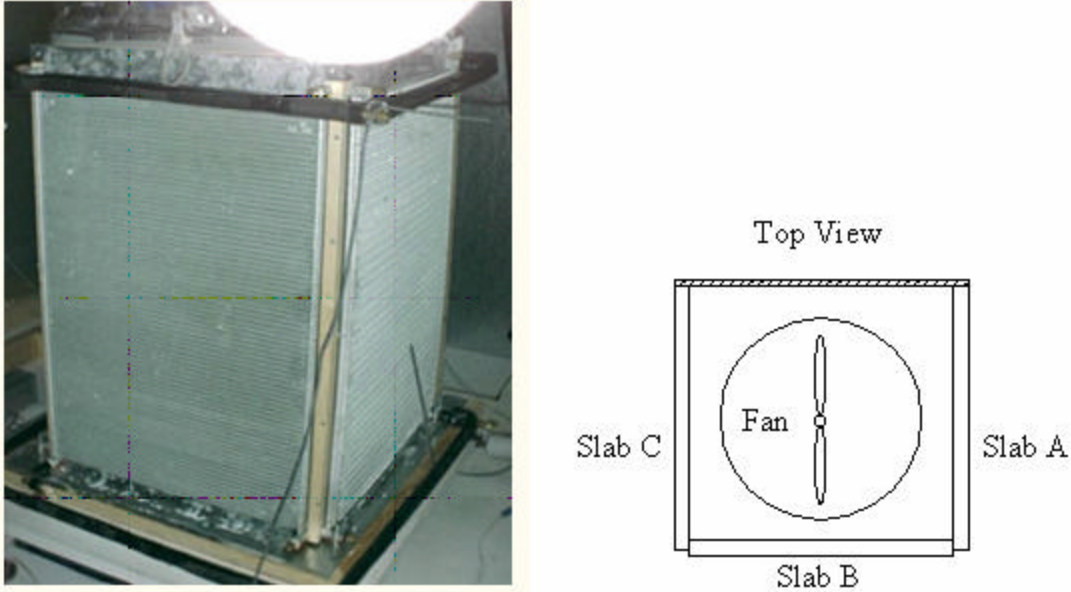


Figure 5.2 Outdoor unit of the prototype R744 heat pump system

Three identical flat microchannel heat exchangers (slabs) are connected in parallel and placed together to form three sides of a box, mimicking U shaped outdoor heat exchangers found in conventional units. The fourth side is closed with plywood. An axial type direct drive fan was mounted on the top of this set of heat exchangers to suck the air through the exchangers. As in the case of conventional finned-tube heat exchangers, the closer to the fan, the higher air face velocity.

Figure 5.3 shows one heat exchanger used in the experiment. Each heat exchanger slab has 80 microchannel tubes divided among six passes, with 16/15/14/14/11/10 tubes per pass. Refrigerant enters the outdoor coil through an inlet elbow, proceeds through six passes and exits through another elbow.

Due to higher operating pressures, the heat exchangers for R744 require either smaller tube diameters or thicker walls. The microchannel heat exchangers have specially designed headers to withstand the higher operating pressures. Figure 5.3 shows the cross-section of heat exchanger header, which has 6 mm tubes closed except for small cutouts at each tube junction. The cross-section of the microchannel tubes used in the heat exchanger and the louvered fin configuration are also shown in Figure 5.3, all dimensions shown on the figure are in mm.

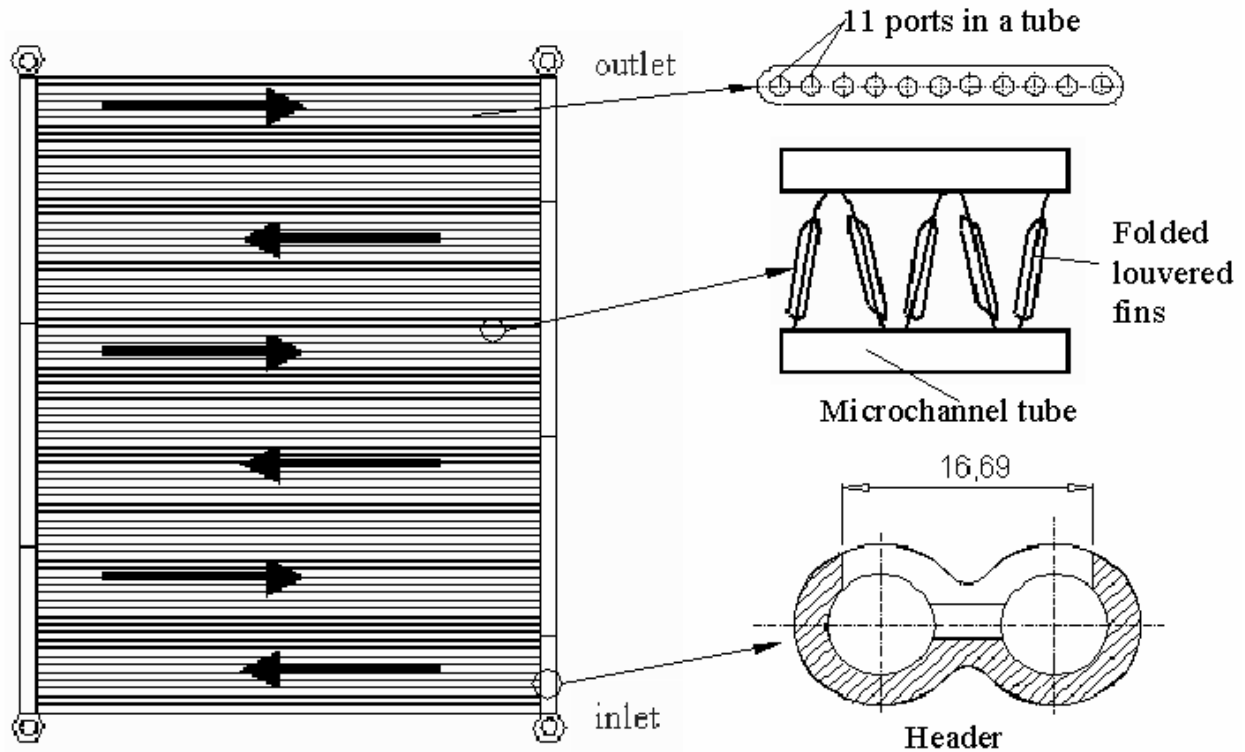


Figure 5.3 Schematic of outdoor heat exchanger

Three manual expansion valves, one for each slab on the outdoor heat exchanger, control refrigerant distribution so exit qualities are equal. The low side accumulator ensures that saturated vapor exits the evaporator at steady state. A suction line heat exchanger is used in the R744 system to obtain refrigerant- and cycle-specific performance improvements that are not available with R410A (see Boewe *et al.*, 1999a, 2001).

The dimensions of the prototype heat exchanger are given in Table 5.1.

Table 5.1 Dimensions and characteristics of outdoor heat exchanger

Outdoor coil Characteristics	
Finned length (m)	0.626
Finned height (m)	0.85
Face Area (cm ²)	5321
Core Depth (cm)	1.65
Core Volume (cm ³)	8780
Airside Area (m ²)	15.02
Refrigerant Side Area (m ²)	1.362
Fin Density (fins/in)	23
Louver Angle (°)	23
Number of Ports	11
Port Diameter (mm)	0.79
Web Thickness (mm)	0.70
Wall Thickness (mm)	0.43
Fin Height (mm)	8.89
Fin Thickness (mm)	0.10
Louver Height (mm)	7.5
Louver Pitch (mm)	0.99
Number of Louvers	2 x 6
Louver redirection Length (mm)	1.7
Louver entry Length (mm)	1.7

5.4 Heat transfer and refrigerant pressure drop test under dry surface condition

Results of experiments in heating mode (Richter *et al.* 2000) were analyzed using a validated simulation model (refer to Chapter 1) and revealed a large discrepancy between calculated and measured outdoor coil performance. Table 5.2 shows the test conditions and Figure 5.4 shows the discrepancy.

Table 5.2 Test conditions for outdoor heat exchanger in heating mode

R744 inlet pressure, Peri	30 ~ 45 bar
Air inlet temperature, Teai	1 ~ 17°C
CO ₂ mass flow rate, mr	13 ~ 25g/s
Airflow rate, mair	500 ~520 g/s (Reynolds number 70)

The air-side heat transfer coefficients were calculated from the experimental data, assuming that refrigerant heat transfer coefficient is known and refrigerant flow is uniformly distributed through the heat exchanger. Figure 5.4 shows that the calculated air-side heat transfer coefficients are about 50% of those calculated using Chang & Wang (1997) correlation. An analysis of experimental uncertainties (see Table 5.3) ruled out measurement errors. Yin *et al.* (2000) compared the predicted results with over 300 experimental data for a transcritical CO₂ gas cooler in a mobile air conditioning system, finding that the model predicted the gas cooler capacity within $\pm 2\%$ using the Chang & Wang (1997) correlation. Our prototype heat exchanger served as a gas cooler during about 70 experiments in cooling mode, so the model was compared to these data, yielding favorable agreement as shown in Figure 5.5. Since the air side heat transfer resistance is dominant for gas coolers, the favorable agreement indicated

that refrigerant-side phenomena must be responsible for the discrepancy noted in Figure 5.4. Since refrigerant-side resistance for CO₂ evaporating in microchannels is extremely small, the evidence pointed to refrigerant maldistribution. Subsequently, a few frosting experiments revealed uneven frosting patterns on all three slabs, with slab B displaying severe maldistribution, which suggested that the refrigerant side distribution for each slab was different.

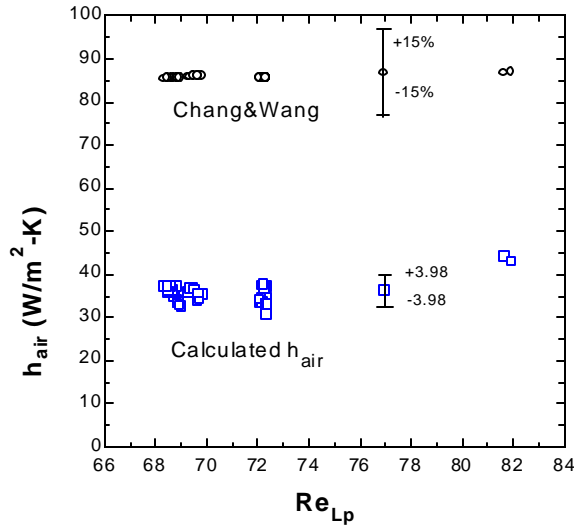


Figure 5.4 Comparison of calculated air side heat transfer coefficient with Chang & Wang correlation

Table 5.3 Uncertainties of measured and calculated parameters

Watt transducer	±0.5%
Glycol mass flow rate	±0.2%
Refrigerant flow rate	±0.2%
Pressure transducer	±0.2%
Thermocouple	±0.5°C
Calculated air-side heat transfer coefficient	±10%

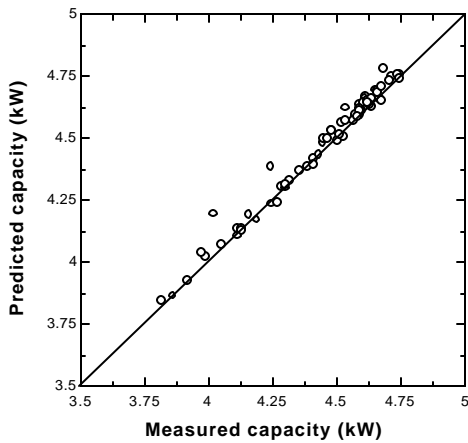


Figure 5.5 Comparison of calculated and measured capacities when the test heat exchanger served as a gas cooler in cooling mode

To explore this further, several experiments were conducted on slab B (middle one) and slab A (right one) separately by reducing compressor speed to reduce the system capacity. In each experiment, a dehumidifier was used to maintain dry surface conditions for comparison with published correlations. Performance of the two heat exchangers was compared at two face velocities, while efforts were made to maintain identical refrigerant flow rates, refrigerant inlet temperatures, and air inlet temperatures

Table 5.4 Test conditions for the slab A and B

At low airflow rate, one blower and one nozzle were used					
	Teai(°C)	Re	V _{air} (m/s)	Teri(°C)	mr(g/s)
Slab A	16.3	71	1.04	8.5	24.9
Slab B	15.6	70	1.02	7.8	23.7
At high airflow rate, two blowers and three nozzles were used					
	Teai(°C)	Re	V _{air} (m/s)	Teri(°C)	mr(g/s)
Slab A	12.5	211	3.1	7.0	28.2
Slab B	12.8	211	3.1	7.2	29.0

Figure 5.6 shows the chamber and airside capacity agree within 5%. Experiments were conducted at eight conditions, including two pairs (at high and low face velocities) data points where equal refrigerant flow rates, refrigerant inlet temperatures, and air inlet temperatures were maintained for the two heat exchangers.

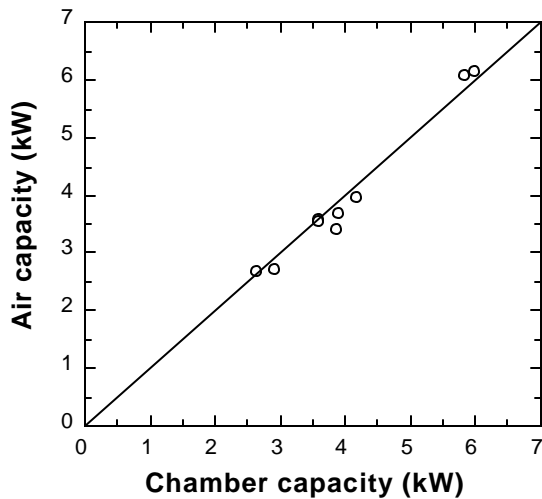


Figure 5.6 Energy balance agreement

Table 5.5 shows the measured and calculated refrigerant pressure drop in the tubes. (The pressure drops in header are neglected in these calculations.) Independent analysis of a similar prototype heat exchanger from the same batch (by Yin *et al.*, 2001) using nitrogen showed that the pressure drops in the header were (as expected) small, but overall pressure drop was much greater than calculated by the model. Subsequent disassembling of the heat exchanger revealed that an average of four ports per tube were blocked and that the actual port diameter was 0.74mm. The asterisk reflects the effect of those assumptions for these heat exchanger slabs.

Table 5.5 Refrigerant pressure drop comparison between slab A and B

At low airflow rate, one blower and one nozzle were used				
	mr(g/s)	Dper(kPa)	Dper _{cal} (kPa)	Dper _{cal} (kPa) [*]
Slab A	24.9	162.0	48.9	134.2
Slab B	23.7	138.9	48.7	133.8
At high airflow rate, two blowers and three nozzles were used				
	mr (g/s)	Dper(kPa)	Dper _{cal} (kPa)	Dper _{cal} (kPa) [*]
Slab A	28.2	174.8	57.9	156.5
Slab B	29.0	207.7	70.5	192.0

Table 5.6 compares measured capacities and calculated air side heat transfer coefficients for slabs A and B. Chamber capacity was used to back out air side heat transfer coefficients assuming that four ports per tube were blocked and the port diameter was estimated 0.74mm. It can be seen that the performance for slab B was much worse than slab A. Moreover the calculated air side heat transfer coefficients for slab A were close to those calculated by Chang & Wang correlation. The disagreement between the model predictions and experimental data for slab B supports the hypothesis that the poor outdoor coil performance may be due to refrigerant maldistribution in slab B.

Table 5.6 Capacity and air side heat transfer coefficient comparison between slab A and B

At low airflow rate: (one blower and one nozzle were used)				
	Q _{chamber} (kW)	Q _{air} (kW)	h _{Chang&Wang}	h _{cal}
Slab A	3.86	3.70	86.5	84.7±28.9
Slab B	2.92	2.73	85.6	32.2±3.9
At high airflow rate: (two blowers and three nozzles were used)				
	Q _{chamber} (kW)	Q _{air} (kW)	h _{Chang&Wang}	h _{cal}
Slab A	5.84	6.11	150.0	113.9±25.2
Slab B	4.16	3.97	150.3	45.9±5.3

5.5 Frosting test

To further understand the nature and extent of refrigerant side causes of capacity degradation in the individual slabs, two cameras were installed to record the frosting process, one in front, and the other behind the heat exchanger. The photos were taken every ten minutes, and all other data were recorded at one-minute intervals. The compressor speed and the expansion valves were adjusted initially to bring the refrigerant temperature slightly below 0 °C. Frost accumulation was observed and heat exchanger performance degradation was monitored until the accumulated frost raised the surface temperature to the dew point of the outdoor air. Then the frosting process stopped. The compressor and valves were adjusted again to further reduce the evaporating temperature and restart the frosting process. Slab A was tested first. It is well known that the flow distribution is strongly affected by the refrigerant inlet mass flux and quality, which influences the flow pattern in the inlet header. To study the effect of inlet quality, two different inlet qualities were tested with same air inlet temperature, air inlet humidity, air flow rate, and refrigerant inlet flow rate.

In the first experiment for slab A with higher inlet quality at approximately 0.3, the air inlet temperature was kept constant at 4.5°C, and the air inlet relative humidity fluctuated around 55±5%. Air flow rate was allowed

to decrease as frost accumulated. The refrigerant inlet flow rate was about 20 g/s and mass flux in the header was about 170 g/s-m². The compressor frequency was 44Hz at the beginning. During the experiment, the expansion valve and compressor were adjusted four times: 50, 100, 140, and 220 minutes after the experiment started. Figures 4 to 6 show the change of important operating variables during the frosting process. The discontinuities reflect periods when the expansion valve and compressor were adjusted.

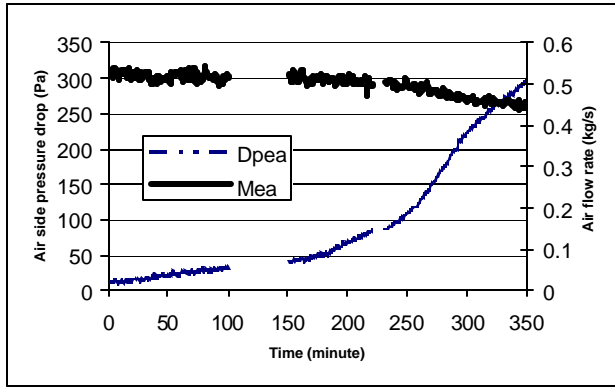


Figure 5.7 Air flow rate and average air pressure drop across the slab A with higher inlet quality (approximately 0.3), keeping blower speed constant

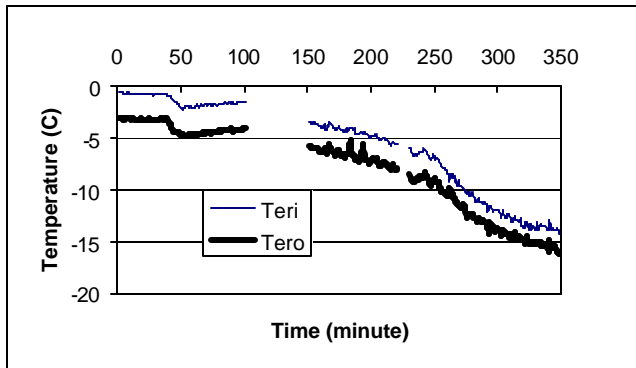


Figure 5.8 Refrigerant inlet and outlet temperature for slab A with higher inlet quality (approximately 0.3)

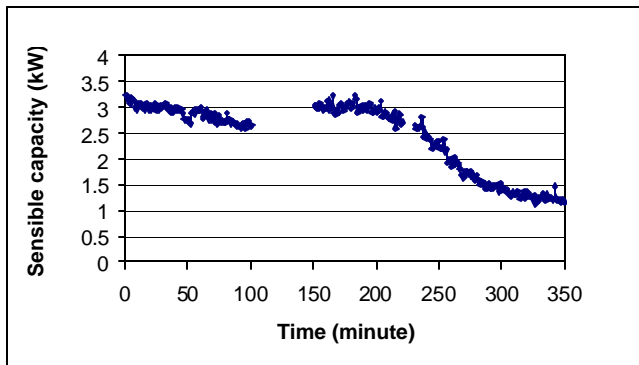


Figure 5.9 Sensible capacity for slab A with higher inlet quality (approximately 0.3)

Figure 5.7 shows the air flow rate and average airside pressure drop across slab A, which increased with frost accumulation. The air flow rate was 0.52 kg/s at the beginning of the experiment and dropped to 0.40 kg/s at the end. The average airside pressure drop was about 12 Pa at the start of the experiment, increased slowly to 40 Pa after 100 minutes. Following further reduction of the evaporating temperature, more frost built up on all the passes and the average airside pressure drop rapidly increased to 300 Pa at the end of the experiment. Figure 5.8 shows the refrigerant inlet and outlet temperature differed by 1~2 °C during the frosting process, which means that we had two-phase at the exit in most of time, and probably fairly uniform temperature. The refrigerant inlet temperature was a little lower than 0 °C at the beginning of the experiment and dropped to approximately -15 °C at the end. Originally, the air velocity at the bottom of the heat exchanger was about half of that at the top. The non-uniformity of air velocity in vertical direction may have some effect on frosting at the start of the experiment. However, refrigerant maldistribution created non-uniform frost deposition, which changed air velocity profile. Frosted areas (with liquid refrigerant) obstructed air flow, increasing air velocities through initially unfrosted regions (where vapor is superheated). That effect increased heat transfer in that non-frosting region and delayed subsequent frosting in that area. Figure 5.9 shows the decrease of sensible capacity during the experiment calculated as follows:

$$Q_{sen} = m_{air} \times Cp \times (T_{ai} - T_{ao}) \quad (5.1)$$

Figure 5.10 shows the frosting photos for slab A with higher inlet quality at approximately 0.3. The photos in Figure 5.10 show that the frosting pattern on the back side of the heat exchanger was the same as that on the front side. This indicates that the port-to-port maldistribution is difficult to characterize due to the high thermal conductivity of the aluminum heat exchanger. Another observation is that there was less frosting on the back side of the heat exchanger than the front side, which can be explained by the decreasing frosting potential from front to back.

Frosting began in the last pass where the refrigerant saturation temperature was lowest due to pressure drop (Figure 5.10, 30 min). After further reducing the evaporating temperature, the frost began to build up on the other passes. In general, the photographs show that the vertical header can produce a fairly uniform refrigerant flow distribution. However it is clear that in some passes some tubes (usually at the bottom or top of each pass) receive less liquid than others, resulting in superheating (hence less frosting) near the tube inlets or outlets. It becomes visible first in exit passes (Figure 5.10, 30 min) and later even in first passes (Figure 5.10, 160 min and 240 min). The maldistribution in the first two passes is hard to detect due to low refrigerant quality in the header. In the third and fourth passes it is obvious that the tubes at the top of the passes received less liquid due to strong effect of gravity. Moving downstream refrigerant quality in the header increases and so does the velocity. Inertial forces play more significant role in determining the flow distribution. As a sequence, we see tubes at the top and bottom of the last pass were fed with less liquid. (Figure 5.10, at 160 and 240 min). The balance between inertial, gravitational and shear forces will determine whether liquid will reach the end of the header section. The following analysis, based on some very crude analytical approximations and ignoring the shear forces, yields some insights into the factors affecting refrigerant flow distribution in the headers of microchannel evaporators.

Since the system was equipped with a well-instrumented suction-liquid line heat exchanger, it was possible to determine the quality of the mixture leaving the evaporator. In the first experiment it varied from 0.30 at the inlet

to 0.95 at the evaporator exit. The two-phase flow in the header is far from being fully developed, but even if it were, its maximum mass flux of $170 \text{ g/m}^2\text{-s}$ would place it in the gravity-dominated regime in each of the headers, with its velocity ranging from a minimum of 0 at the top and bottom of each header segment, to reaching a maximum at the point in the header where the flow switches from exiting to entering the tubes.

Continuing with the fiction of homogeneous flow, and assuming constant heat flux over the entire crossflow heat exchanger, we can roughly estimate the maximum velocities in each header section: 0.7, 0.9, 1.0, 1.2, 1.4 and 1.6m/s, respectively. Using these maximum velocities and equating kinetic to potential energy, we find that the fluid in the lower (low quality) headers may lack the momentum required to carry it to the top (the next baffle). Therefore it is possible that liquid refrigerant accumulates in the lower-quality headers, while bubbles churn the flow and propel droplets upwards where they are drawn into the tubes. The resulting frosting patterns in the lower headers are more uniform in the second experiment shown in Figure 5.11 where quality varied from 0.15-0.85, as would be expected.

The photos in Figure 5.10 show that the higher the quality in the header, the more uneven the frosting becomes and the more obvious maldistribution is. In the headers near the top of the heat exchanger, the kinetic energy is large enough to propel the droplets 10-15 cm vertically, theoretically enough to reach the upper baffles. Perhaps due to droplet size distributions, insufficient liquid reaches the top tubes, as is clearly visible in both experiments. Moreover, partially superheated tubes are also visible at the bottom tubes of the upper headers, suggesting that there is no column of standing liquid in these higher-velocity headers, and that liquid droplets bypass the lower tubes before turning into the middle ones. This is to be expected because the liquid-vapor density ratio for R744 is about 9; the angular momentum required for liquid to make a 90-degree turn is 9 times greater than for vapor. Near the center of the pass, the velocity is lower by a factor of 2, and the centripetal force is reduced by a factor of 4, making it easier for the droplets to turn into the tubes at the center of the pass.

Since the flow is actually nonhomogeneous, not fully developed, and not steady, further understanding of the distribution mechanisms await the development of more sophisticated measurement techniques. For example Peng *et al.* (2002) are studying two-phase flow distribution in transparent horizontal header using a phased Doppler particle analyzer to measure velocity, size and distribution of droplets. They found that when the refrigerant inlet quality reached 0.8 in upward flow, “vapor disturbance effects” become significant, and the vapor hindered the liquid from entering the first channels.

Figure 5.11 shows the frosting photos for the second experiment conducted at the same refrigerant flow rate, where the inlet and exit qualities were lower (approximately 0.1 at the inlet and 0.85 at the outlet), and the distribution correspondingly better. The air inlet temperature in the second experiment was kept constant at $5.5 \text{ }^\circ\text{C}$, and the air inlet relative humidity fluctuated around $55 \pm 5\%$ while the air flow rate dropped from 0.52 kg/s at the beginning of the experiment to 0.36 kg/s at the end. The maldistribution was not obvious in the first four passes. In the last pass the top and bottom tubes received less liquid as discussed above. Figures 5.12 and 5.13 show the refrigerant temperature and sensible capacity from the second experiment.

Figure 5.14 shows the frosting photos for slab B (middle one), for which the measured performance under dry conditions was much worse than the other two slabs. A manufacturing defect was suspected, and the frosting

experiments tend to confirm it. Even at the beginning (Figure 5.14, 30 min) some unexpected frosting patterns are visible. It is stronger at 90 min. It is obvious that there is liquid in the first and second passes. The third pass has less liquid than expected. And there is almost no frost at all in the fourth pass indicating a deficiency of liquid. However, liquid is present in the fifth pass and disappears again in the sixth pass. It appears that the baffles between the third and fourth passes as well as fifth and sixth passes were improperly installed, allowing liquid to bypass an entire set of tubes. As a consequence, there is a significant region of superheated vapor in the fourth and six passes which causes the deterioration of the performance of the whole coil. At some point the heat exchanger will be cut apart to confirm this hypothesis.

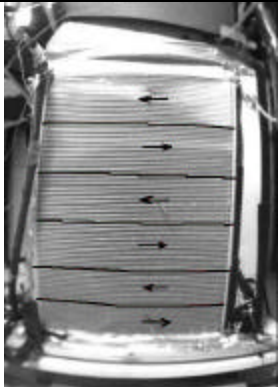
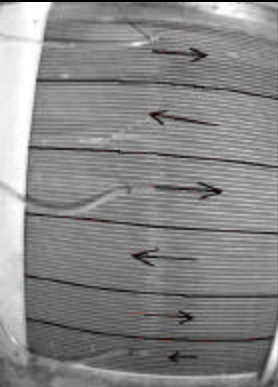
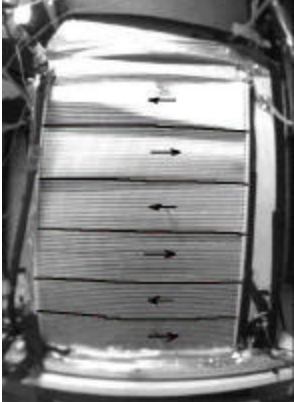
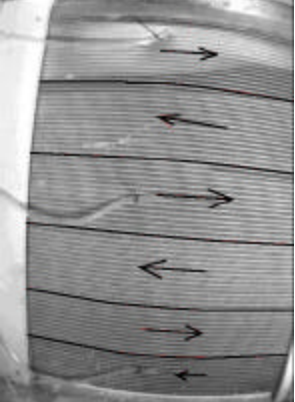

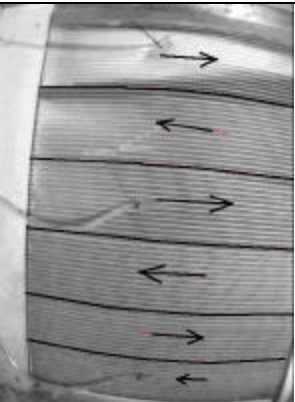

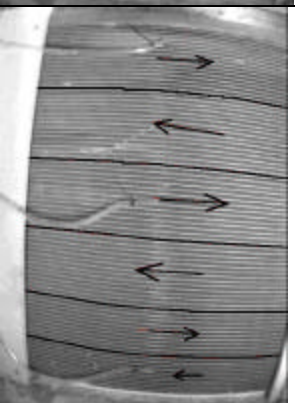
	Front		Back		
Out — In —				— Out In —	30 min
					160 min
					240 min
					300 min

Figure 5.10 Frosting of a slab A (right slab) with higher inlet quality at approximately 0.3

	Front		Back	
Out — In —				— Out In

Figure 5.11 Frosting of a slab A (right slab) with lower inlet quality at approximately 0.1

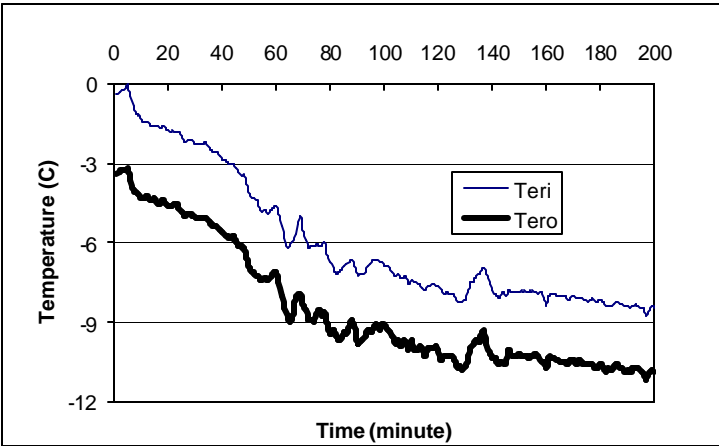


Figure 5.12 Refrigerant inlet and outlet temperature for slab A with lower inlet quality (approximately 0.1)

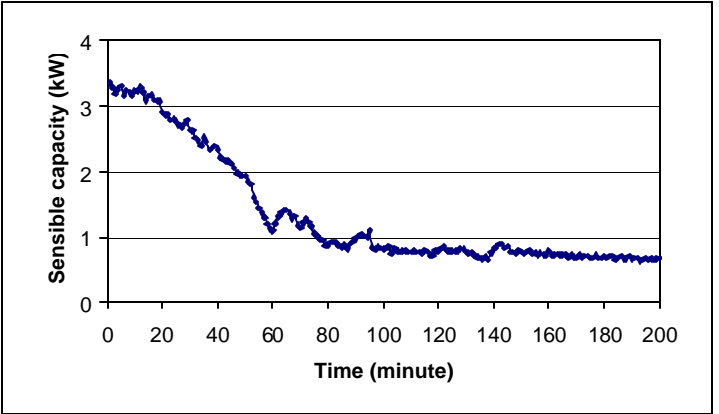


Figure 5.13 Sensible capacity for slab A with lower inlet quality (approximately 0.1)

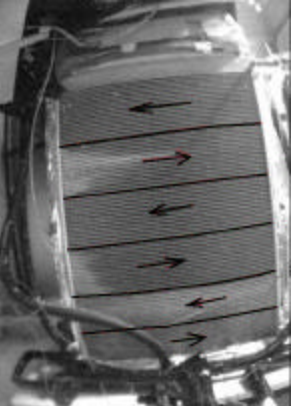
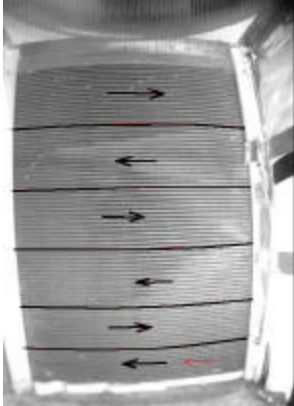
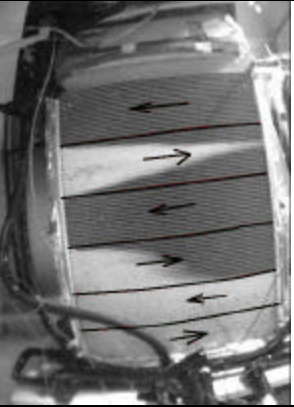
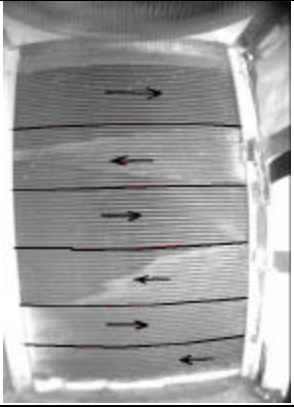
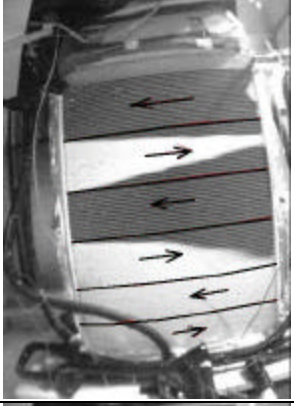
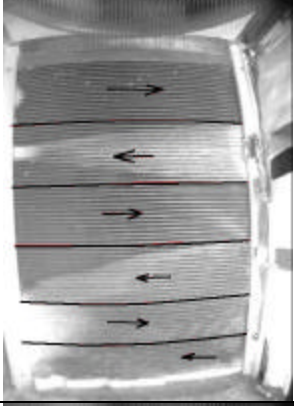
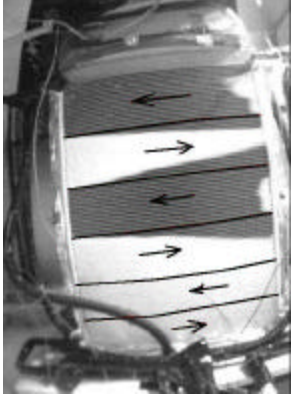
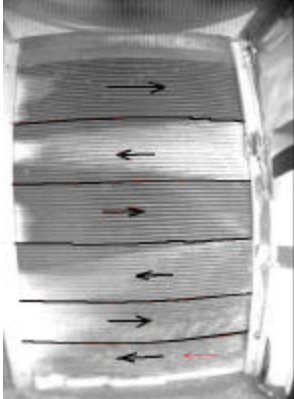
	Front		Back		
Out —				— Out	30 min
In —				In —	
					90 min
					160 min
					220 min

Figure 5.14 Frosting of a slab B (middle slab)

5.6 Conclusion

Two-phase flow distribution of CO₂ in a microchannel evaporator with vertical header using frosting has been investigated. It appears that vertical headers can produce a fairly uniform refrigerant flow distribution. In some passes, the tubes near the bottom or top usually received less liquid than others, and the location of these tubes is determined by the balance between inertial, gravitational and shear forces. The refrigerant flow in the low-quality headers was gravity dominated, and moving downstream, inertial forces in the headers play more significant role in determining the flow distribution. The refrigerant flow distribution, as indicated by frost patterns, is more uniform when the inlet quality is low. Refrigerant maldistribution created a non-uniform frost deposition, which increased air velocity through regions where the surface was initially unfrosted (e.g. where vapor was superheated). That effect increased heat transfer in non-frosting region and slowed down subsequent frosting in that area.

A manufacturing problem (faulty baffles that created refrigerant flow shortcuts) was clearly identified, demonstrating that frosting technique is an inexpensive and efficient tool to visualize and characterize refrigerant maldistribution problems.

References

- Aarde, D.J. and Kroger, D.G., 1993, "Flow Losses Through an Array of a-Frame Heat Exchangers", *Heat Transfer Engineering*, Vol. 14, No. 1, pp. 43-51.
- ARI 1987, Forced-Circulation Air-Cooling and Air-Heating Coils, *ARI Standard 410-87*, Air-Conditioning and Refrigeration Institute.
- Beaver, A.C., J. M. Yin, C. W. Bullard, P. S. Hrnjak. 1999. Experimental and Model Study of the Heat Pump/Air Conditioning Systems Based on Transcritical Cycle with R744. *IIR Congress*, Sidney, Australia
- Beaver, A.C., J. M. Yin, C. W. Bullard, P. S. Hrnjak. 1999a. An Experimental Investigation of Transcritical Carbon Dioxide Systems for Residential Air Conditioning. University of Illinois at Urbana-Champaign, *ACRC CR-18*.
- Boewe, D., C. W. Bullard, J.M. Yin, P.S. Hrnjak, 2001. Contribution of Internal Heat Exchangers to Transcritical R-744 Cycle Performance. *HVAC&R Research*, Vol.7, No.2, 2001, p155-168
- Boewe, D., J. M. Yin, Y. C. Park, C. W. Bullard, P. S. Hrnjak. 1999. The Role of the Suction Line Heat Exchanger in Transcritical R744 Mobile A/C Systems. *SAE paper 1999-01-0583*
- Boewe, D. E., McEnaney, R.P., Park, Y.C., Yin, J.M., Bullard, C.W. and Hrnjak, P.S., 1999, "Comparative Experimental Study of Subcritical R134a and Transcritical R744 Refrigeration Systems for Mobile Applications," *ACRC CR-17*, University of Illinois at Urbana-Champaign.
- Chang, W.R., Wang, C.-C., and Chang, Y.J. 1994, "Effect of an Inclination Angle on the Heat Transfer and Pressure Drop Characteristics of a Wavy Finned-Tube Heat Exchanger," *ASHRAE Trans.*, Vol. 100, Pt. 2, pp. 826-832.
- Chang, Y. and Wang, C., 1996, "Air Side Performance of Brazed Aluminum Heat Exchangers," *Journal of Enhanced Heat Transfer*, Vol. 3, No. 1, pp. 15-28.
- Chang, Y. and Wang, C., 1997, "A Generalized Heat Transfer Correlation for Louvered Fin Geometry," *Int. J. Heat Transfer*, Vol. 40, No. 3, pp. 533-544.
- Chiou, C.B., Wang, C.C., Chang, Y.J. and Lu, D.C., 1994, "Experimental Study of Heat Transfer and Flow Friction Characteristics of Automotive Evaporators," *ASHRAE Trans.*, Vol. 100, Pt. 2, pp. 575-581.
- Choi, Steve H. Shin, Sehyun. Cho, Young I. "Effect of Area Ratio on the Flow Distribution in Liquid Cooling Module Manifolds for Electronic Packaging", *International Communications in Heat & Mass Transfer*. v 20 n 2 Mar-Apr 1993. p221-225
- Fei, P., Canfrak, Di, P. S. Hrnjak. Refrigerant Distribution in the Headers of Plate Evaporators, *SAE Paper 02HX47*, to be published at SAE 2002 World Congress.
- Giannavola, M.S., Experimental Study of System Performance Improvements in Transcritical R744 Systems for Mobile Air-Conditioning and Heat Pumping, *ACRC CR-46*, University of Illinois at Urbana-Champaign.
- Hwang, Y., 1997, "Comprehensive Investigation of Carbon Dioxide Refrigeration Cycle," *Ph.D. Thesis*, University of Maryland.
- Kariyasaki, Akira. Nagashima, Tohru. Fukano, Tohru. Ousaka, Akihara. "Flow Separation Characteristics of Horizontal Two-Phase Air-Water Flow into Successive Horizontal Capillary Tubes Through T-Junction", *ASME/JSME Thermal Engineering Joint Conference Proceedings*. v2 1995. ASME, New York, NY, USA. p 75-82
- Kim, Sooyoun. Choi, Eunsoo. Cho, Young I. "Effect of Header Shapes on the Flow Distribution in a Manifold for Electronic Packaging Applications", *International Communications in Heat & Mass Transfer*. v 22 n 3 May-Jun 1995. p 329-341
- McElgin, J. and Wiley, D. 1940, "Calculation of Coil Surface Areas for Air Cooling and Dehumidification," *Heating, Piping and Air-Conditioning*, March, pp. 195-201.
- McQuiston, F.C. 1975, "Fin Efficiency with Combined Heat and Mass Transfer," *ASHRAE Trans.*, vol.81, pt. 1, pp. 350-355.

- Richter, M.R., S.M. Song, J.M. Yin, M.H. Kim, C.W. Bullard, P.S. Hrnjak, "Transcritical CO₂ Heat Pump for Residential Application", *4th IIR-Gustav Lorentzen Conference on Natural Working Fluids*, Purdue University, July, 2000.
- Rong, Xiaoyang. Kawaji, Masahiro. Burgers, John G. "Two-phase Header Flow Distribution in a Stacked Plate Heat Exchanger", *Gas Liquid Flows American Society of Mechanical Engineers, Fluids Engineering Division* (Publication) FED. v 225 1995. ASME, New York, NY, USA. p 115-122
- Souza, A.L. and Pimenta, M., 1995, "Prediction of Pressure Drop During Horizontal Two-Phase Flow of Pure and Mixed Refrigerants," *ASME Symposium Series*, FED-Vol. 210.
- Stoecker, W. and Jones, J. 1982, *Refrigeration and Air conditioning*, McGraw-Hill, New York.
- Threlkeld, J. L. 1970, *Thermal Environmental Engineering*, Prentice-Hall, New Jersey
- Watanabe, Manabu. Katsuta, Masafumi. Nagata, Katsuya. "Two-phase Flow Distribution in Multi-pass Tube Modeling Serpentine Type Evaporator", *ASME/JSME Thermal Engineering Joint Conference - Proceedings*. v 2 1995. ASME, New York, NY, USA. p 35-42
- Yin, J. M., C. W. Bullard, and P. S. Hrnjak, 2000, "Design Strategies for R744 Gas Coolers," *Proceedings of the IIF-IIR Commission B1, B2, E1, and E2*, Purdue University, W. Lafayette, IN, 315-322, July.
- Yin, J.M., 1999, "Model for CO₂ Evaporator", *Technical Memo #26*, Air Conditioning and Refrigeration Center, University of Illinois at Urbana-Champaign.
- Yin, J.M., Hrnjak, P.S. and Bullard, C.W., 2000, "Development and Validation of a R744 Gas Cooler Model," *ACRC Technical Report*, Air Conditioning and Refrigeration Center, University of Illinois at Urbana-Champaign.
- Zivi, S.M., 1964, "Estimation of Steady-State Steam Void Fraction by Means of the Principle of Minimum Entropy Production", *Journal of Heat Transfer*, Vol.86, pp.247-252.